




# JGR Space Physics



## RESEARCH ARTICLE

10.1029/2024JA033320

# Impact of Sudden Stratospheric Warming and Elevated Stratopause Events on the Very Low Frequency Radio Signal

H. Schneider<sup>1</sup> , V. Wendt<sup>1</sup> , D. Banyś<sup>1</sup>, M. Hansen<sup>1</sup>, M. Clilverd<sup>2</sup> , and P. T. Verronen<sup>3,4</sup>

<sup>1</sup>German Aerospace Centre, Solar Terrestrial Institute, Neustrelitz, Germany, <sup>2</sup>Physical Sciences Division, British Antarctic Survey, Cambridge, UK, <sup>3</sup>Sodankylä Geophysical Observatory, University of Oulu, Sodankylä, Finland, <sup>4</sup>Space and Earth Observation Centre, Finnish Meteorological Institute, Helsinki, Finland

### Key Points:

- The average VLF amplitude during three Sudden Stratospheric Warming (SSW)/Elevated Stratopause (ES) events is increased (SSW)/decreased (ES)
- Changes in temperature, H<sub>2</sub>O and NO during the SSW/ES events are identified as initial drivers of the VLF amplitude perturbations
- The collision frequency, Ne and VLF signal absorption are modified by atmospheric drivers resulting in observed VLF amplitude perturbations

### Supporting Information:

Supporting Information may be found in the online version of this article.

### Correspondence to:

H. Schneider,  
helen.schneider@dlr.de

### Citation:

Schneider, H., Wendt, V., Banyś, D., Hansen, M., Clilverd, M., & Verronen, P. T. (2025). Impact of sudden stratospheric warming and elevated stratopause events on the very low frequency radio signal. *Journal of Geophysical Research: Space Physics*, 130, e2024JA033320. <https://doi.org/10.1029/2024JA033320>

Received 16 SEP 2024

Accepted 4 MAR 2025

### Author Contributions:

**Conceptualization:** H. Schneider, V. Wendt, D. Banyś

**Data curation:** V. Wendt, M. Hansen, M. Clilverd, P. T. Verronen

**Formal analysis:** H. Schneider

**Investigation:** H. Schneider

**Methodology:** H. Schneider, V. Wendt

**Resources:** M. Hansen, M. Clilverd, P. T. Verronen

**Software:** H. Schneider, M. Hansen

**Supervision:** V. Wendt, D. Banyś

**Validation:** H. Schneider

**Writing – original draft:** H. Schneider

**Abstract** Sudden Stratospheric Warmings (SSW) and Elevated Stratopause (ES) events are mid-to-high latitudinal, atmospheric wave-driven phenomena leading to significant changes in wind, temperatures, and vertical mass transport, especially at stratospheric and mesospheric altitudes. Presumably, SSW and ES-induced changes also cause modifications in the highly variable D-region ionization. This bottom side of the ionosphere behaves with the Earth's surface as a reflection boundary for Very Low Frequency (VLF) radio signal transmission used for long-distance communication. Since perturbations of the D-region ionization are also notable in the VLF signal, it is a valuable tool for continuous investigations of the D-region. Here, we study the impact of four SSW/ES events on the VLF signal amplitude between the high latitude transmitter-receiver link Keflavik, Iceland, to Ny-Ålesund, Svalbard, to gain further knowledge about interactions between the D-region and the atmosphere during these atmospheric phenomena. For three of four SSW/ES events, a very similar VLF signal amplitude signature is observed, characterized by a significant increase during the SSW period in the signal amplitude followed by a decrease during the ES period. This study aims to reveal a possible mechanism driving these similar VLF signal amplitude variations, involving modified electron neutral collision frequencies and electron densities due to changed temperatures and minor constituent concentrations according to the SSW/ES events. However, the VLF signal amplitude for one event increased 2 weeks later than during the other three events and did not show a decrease during the ES period. Possible causes for the different VLF signal amplitude variations are discussed.

**Plain Language Summary** Man-made radio signal transmissions with low frequencies (VLF, 3–30 kHz) travel from transmitter to receiver by being reflected between the Earth's surface and the bottom side of the ionosphere (D-region, 60–90 km). Since the D-region is the VLF's upper reflection boundary, its ionization perturbations are notable in the VLF signal amplitude. The highly variable ionization can be affected by atmospheric phenomena like Sudden Stratospheric Warmings (SSW) and Elevated Stratopause (ES) events. The wave-driven SSW/ES events occur in mid-to-high latitudes and cause significant changes in wind, temperatures, and vertical mass transport. For three SSW/ES events, a similar VLF signal amplitude signature is observed for a high-latitude transmitter-receiver link, characterized by a significant increase during the SSW period in the signal amplitude followed by a decrease during the ES period. Changes in temperature, water vapor, and nitric oxide are considered initial causes for the observed amplitude anomalies, affecting the vertical electron density profile and signal absorption. However, the VLF signal amplitude for one event does not show the characteristic increase/decrease during the SSW/ES period. We assume that the difference is caused by a combination of enhanced wave activity and a modified nitric oxide concentration.

## 1. Introduction

Man-made radio waves with very low frequencies (VLF, 3–30 kHz) can travel long distances up to 20,000 km from transmitter (Tx) to receiver (Rx) with low attenuation of  $\sim 2\text{--}3\text{ dB} \cdot \text{Mm}^{-1}$  (Hunsucker & Hargreaves, 2002; Wait, 1957). Furthermore, they have a relatively large skin depth in seawater (Barr et al., 2000), leading to their primary usage for naval communication. For this purpose, a global network of transmitters and receivers was set up to ensure good data coverage with continuous measurements. While propagating from the transmitter to the receiver, VLF waves are reflected between the Earth's surface and the D-region, the so-called earth-ionosphere waveguide. By this, changes in the D-region ionization are notable in the amplitude as well as the phase of the VLF signal. The D-region is the ionosphere's lowest part, ranging from  $\sim 60\text{--}90\text{ km}$  during the day and forms back to  $\sim 75\text{--}90\text{ km}$  at night. The diurnal variation in the height of the lower D-region boundary is due to different

©2025. The Author(s).

This is an open access article under the terms of the [Creative Commons Attribution License](https://creativecommons.org/licenses/by/4.0/), which permits use, distribution and reproduction in any medium, provided the original work is properly cited.

Writing – review & editing: V. Wendt,  
D. Banyś, M. Hansen, M. Clilverd,  
P. T. Verronen

ionization sources at night and daytime. During the daytime, the primary ionization sources are the photoionization of nitric oxide (NO) by Lyman- $\alpha$  radiation and, below 70 km, the ionization of neutral components by cosmic galactic rays (Thomson et al., 2022). During the night, there is no direct solar radiation. Lyman- $\alpha$ , backscattered from the neutral hydrogen in the Earth's geocorona, is the primary ionization source at low and middle latitudes. At higher latitudes, galactic cosmic rays play a vital role (Thomson et al., 2021). The production of free electrons in the D-region competes continuously with electron loss mechanisms, which are affected by the minor constituents oxygen (O), water vapor (H<sub>2</sub>O), and ozone (O<sub>3</sub>) (Mitra, 1978). Due to its high recombination rates, the ionization of the D-region is very sensitive to changes. Perturbations in the D-region ionization can have a solar or geomagnetic origin, for example, solar flares (Grubor et al., 2008; Wenzel et al., 2016), gamma-ray bursts (Mondal et al., 2012), or geomagnetic storms (Mondal et al., 2021). However, the D-region can also be disturbed by drivers from below, for example, planetary waves (Schmitter, 2011), volcano eruptions (Solovieva & Shalimov, 2022), or sudden stratospheric warmings (Pal et al., 2017).

SSWs are atmospheric phenomena generated by the interactions between the background wind and upwards propagating planetary waves (e.g., Andrews et al., 1987; Matsuno, 1971, and others). Since planetary waves can only propagate upwards when the zonal background wind is eastward (Charney & Drazin, 1961), SSWs preferably occur during wintertime in higher latitudes where the polar vortex with its westerly winds develops. SSWs are characterized by a sudden increase in stratospheric temperatures (mainly at altitudes between 30 and 50 km) and a simultaneous decrease at mesospheric temperatures (approximately 60–90 km). In addition, the eastward background wind weakens at stratospheric and mesospheric altitudes and reverses in strong cases. SSW events are commonly classified into minor and major warmings. Both minor and major warmings show a strong warming of the stratosphere in higher latitudes (>60°) at 10 hPa. However, for a major warming event, the zonal background wind must also be reversed in 10 hPa from eastward to westward (Baldwin et al., 2021). The zonal wind reversal during SSW events prevents the planetary waves (PW) from propagating further into the stratosphere. Also, the wind reversal alters filter conditions for the gravity wave (GW) propagation into the mesosphere. The modified filter conditions for GW result in changes in the strength and direction of the GW-driven residual mesospheric circulation from the summer to the winter pole and cause, in some cases, a significant rise in the stratopause (Scheffler et al., 2022). That rise of the stratopause is a so-called elevated stratopause (ES) event. It is manifested by a vanishing of the stratopause and a reformation a couple of days later at higher altitudes (70–80 km), from where it slowly descends to usual altitude ranges (approximately 50–60 km). The mesosphere's characteristic warming and the stratosphere's cooling during an ES event are accompanied by strong eastward zonal mesospheric winds (Chandran, Collins, et al., 2013; Limpasuvan et al., 2016; Manney et al., 2005). In addition to the changes in zonal wind and temperature, SSW and ES events are also characterized by changes in vertical transport. During SSW/ES, there is increased upwelling/downwelling in mesospheric regions (60–90 km), which leads to vertical mass transport, causing altitude-dependent changes in the trace gas concentrations (Chandran et al., 2014; Manney et al., 2009).

In studies, it is common sense that ES events occur mainly after prolonged major SSWs. They are primarily formed by adiabatic heating from the downwelling branch of the changed residual circulation. Those changes in the residual circulation are driven by GW and/or PW (Chandran, Garcia, et al., 2013; Limpasuvan et al., 2016; Okui et al., 2021). To which contribution GW and PW play a role in the ES formation is highly discussed. Yamashita et al. (2013) agrees with Siskind et al. (2018) and Chandran, Collins, et al. (2013) in the assumption that non-orographic GW force plays a crucial role in the formation and the descent of the elevated stratopause. In contrast, Karami et al. (2023) showed with UA-ICON simulations that an ES forms even in the complete absence of GWD, indicating that the non-orographic GW is not the only driver for the ES formation. Furthermore, Yamashita et al. (2013) stated that the drag of meridional propagating GW also contributes to the formation of the ES, which is supported by SABER GW variations and ray-tracing simulations. The role of PW in the initial phase of the ES has been discussed in several studies (Chandran, Collins, et al., 2013; Chandran et al., 2011; Limpasuvan et al., 2012, 2016). A composite study of 13 SSW/ES events with SD-WACCM runs reveals a negative PWF in the polar mesosphere/lower thermosphere (MLT), inducing a downward flow as the origin for the ES formation (Limpasuvan et al., 2016). A recent study of Okui et al. (2021) represents a mechanism for ES formation, assuming that the drag of both GW and PW is essential. The variety of likely drivers for the ES formation shows that the contributions of the PW and GW and their interplay are not fully understood due to diverse difficulties, for example, the lack of global GW observations in the MLT (Yamashita et al., 2013) or the

limitations of reanalysis data by the upper lid of most reanalyses in around or below 0.01 hPa ( $\approx 80$  km) (Karami et al., 2023). Further investigations are required.

There are only a few studies on the effects of SSW on the VLF signal. Almost 60 years ago, Belrose (1967) reported decreased VLF phase height and enhanced absorption of the medium MF signal (300 kHz–3 MHz) during the SSW in 1952. Larsen (1971) investigated the impact of the SSW event in 1969 on the short path VLF signal at high latitudes in combination with ionosonde data and couldn't note a significant change in the electron density profile. In Clilverd et al. (2006, 2007a) SSWs were considered indirectly by analyzing the influence of the polar vortex strength (which is weakened by SSW events) and the occurrence of solar proton events on the descent of the high-altitude odd nitrogen,  $\text{NO}_x$  ( $\text{NO} + \text{NO}_2$ ). From the variability of the difference between the midday and midnight VLF signal amplitudes for several winter periods, they concluded that the combination of strong  $\text{NO}_x$  sources as solar proton events and a strong polar vortex is required to enhance the  $\text{NO}_x$  concentration in the mesosphere and stratosphere. Pal et al. (2017) investigated the impact of the SSW event in 2009 on the VLF signal of six mid- to high-latitude links and found a significant effect on the VLF (3–30 kHz)/LF (30–300 kHz) signal amplitudes during the SSW event, which was very different for the different links. Sen et al. (2024) gained similar results by studying the impact of the SSW event in 2018 on five different mid-latitude links. Both assume that modifications of the lower ionospheric electron density and electron-neutral collision frequency profiles during the SSW event cause modal interference effects between the different waveguide modes, resulting in changed amplitudes. They discussed atmospheric wave interactions as the primary source for the modifications of the ionospheric perturbations. The previous studies focused on the effects of SSW on the VLF signal. To date, the effects of an ES event on the VLF signal have not been investigated, nor have SSW and ES been considered separate events. In addition, the impact of various SSW/ES events on one Tx-Rx link has not yet been taken into account to derive an average signature.

This paper investigates the effects of four SSW/ES events on the daytime VLF signal amplitude under low/moderate solar activity for the high-latitude link from Keflavik, Iceland, to Ny-Ålesund, Svalbard. In Section 2, the different data sources are introduced. For better comparability, a mesospheric onset day is defined in Section 3 to center the SSW/ES events. Subsequently, the temporal development of the VLF amplitude, the most likely atmospheric drivers, and the averaged behavior are presented for all four events. The results and a possible mechanism are discussed in Section 4, and finally, conclusions are drawn in Section 5.

## 2. Data and Methods

### 2.1. VLF Signal Amplitude

It's important to note that the SSW/ES induced changes in mesospheric temperatures, wind, and neutral composition occur in the same altitude ranges as the aforementioned ionospheric D-region. This suggests that SSW/ES events could potentially cause perturbations of the sensitive D-region ionization, consequently resulting in perturbations of the VLF signal. To investigate the impact of SSW/ES events on the VLF signal in high latitudes, we analyze the amplitude of the narrow band VLF signal transmitted from Keflavik, Iceland (call-sign: NRK) and received in Ny-Ålesund, Svalbard (NYA). The pathway is shown in Figure 1. The transmitter NRK operates at 37.5 kHz. The receiver site is part of the Antarctic Arctic Radiation-belt Dynamic Deposition VLF Atmospheric Research Konsortia (AARDDVARK), which provides a network of continuous long-range observations of the lower ionosphere in the polar regions (Clilverd et al., 2009). The link NRK-NYA was chosen since its 2,000 km long pathway lies within the high latitudes, where SSW and ES events show the strongest impact. In addition, this link has a long period of continuous data coverage (from 2006), which enables investigating multiple SSW/ES events. In this study, we focus on only one link and consider various events, so differences in the technical setup can be excluded as a cause for different VLF signal amplitude variations during the SSW/ES events. The receivers from AARDDVARK are able to record the amplitude and phase of Minimum Shift Keying (MSK) modulated VLF radio transmission (Clilverd et al., 2009). 10-minute medians of the raw VLF signal amplitude are used to reduce short-term fluctuation, for example, caused by solar flares. For the analysis, the 10-min medians are processed to level the artificial amplitude jumps caused by maintenance action and to filter the outlier. The detailed description of the processing of the VLF signal amplitude to so-called level 2 data is described in Schneider et al. (2024).

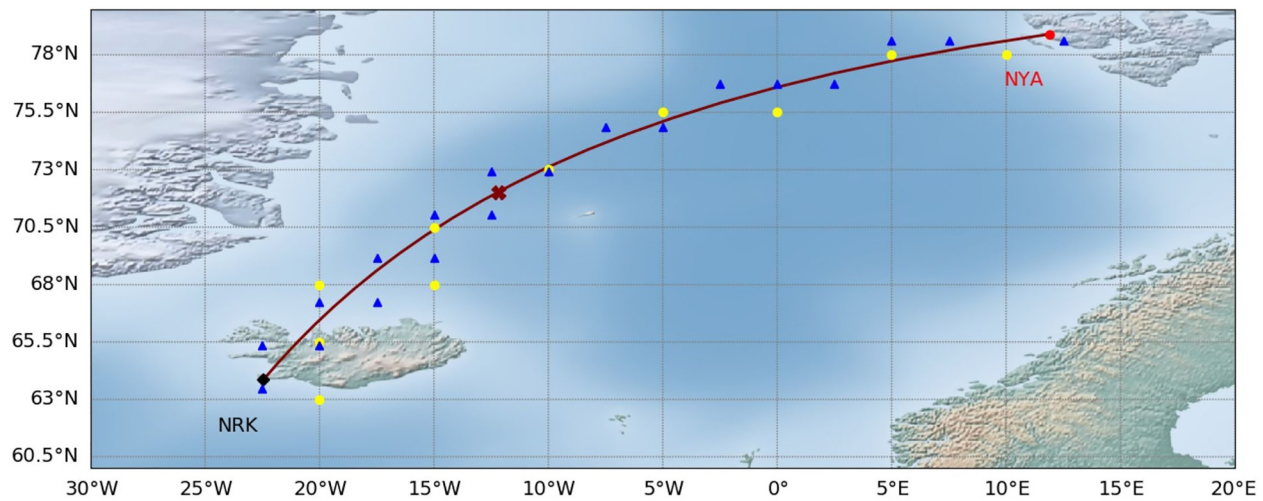


**Figure 1.** Pathway from transmitter NRK to receiver NYA. The interpolation grid for the MLS raw data is shown in gray. Yellow dots mark grid points for MLS parameter and blue triangles mark grid points for SD-WACCM-X parameter computation. The maroon cross marks the position of the pathway midpoint (72.03°N, 12.2°W).

## 2.2. Atmospheric Parameters From MLS

As an SSW/ES event is an atmospheric phenomenon manifested by significant changes in temperature, dynamics, and chemistry, various atmospheric parameters are compared with the VLF signal in this study. Temperature and zonal wind were chosen since their modification defines the SSW/ES event. This study uses neutral temperature [K], H<sub>2</sub>O volume mixing ratio (VMR) [ppmv], and O<sub>3</sub> [VMR, ppmv] data from the Microwave Limb Sounder (MLS) on board the Aura satellite (Livesey et al., 2015; Waters et al., 2006). The zonal wind was computed with the geostrophic wind balance equation using the geopotential height provided by MLS (Rüfenacht et al., 2018). MLS moves on a sun-synchronous polar orbit and covers latitudinal ranges from 82°N to 82°S. It was launched in July 2004, and since August 2004, data with a temporal resolution of 1 day at each location are available. The altitudinal resolution descends with increasing altitudes with ~4 km in the stratosphere and ~14 km at mesopause altitude ranges. Generally, the useable height range of the MLS observations goes from 11 to 97 km (261–0.001 hPa). Version 5 MLS data were used, and the most recent recommended quality screening procedures of Livesey et al. (2015) have been applied. The Version 5 MLS raw data were clustered into grid boxes with dimensions of 5° in longitude and 2.5° in latitude. For each grid box, the final grid value is computed by inverse distance-weighted smoothing method for every day (Brakebusch et al., 2013). We used grid points closest to the VLF signal propagation path from NRK-NYA for our analyses, as shown in Figure 1 (yellow points).

## 2.3. Nitric Oxide From the SD-WACCM-X

This study uses specified dynamics simulations of the numerical model Specified Dynamics Whole Atmosphere Community Climate Model eXtended Version (SD-WACCM-X). WACCM-X simulates the atmosphere from the Earth's surface up to 500–700 km under consideration of chemical, physical, and dynamical processes, as well as the coupling of the atmosphere with the ocean, sea ice, and land. WACCM-X combines the whole atmosphere community climate model for the atmospheric component (Marsh et al., 2013) and the thermosphere ionosphere electrodynamics general circulation models for the ionospheric processes (TIE-GCM; Richmond et al., 1992). More details about the model with thermosphere and ionosphere extension can be found in Liu et al. (2018). In SD-WACCM-X simulations, WACCM-X is constrained by realistic temperature and wind data from Modern-Era Retrospective analysis for Research and Applications version 2 (MERRA-2; Rienecker et al., 2011). SD-WACCM-X provides global NO volume mixing ratio (VMR) data with a horizontal resolution of the grid is 1.9° in latitude and 2.5° in longitude with 145 levels in the vertical direction with a resolution of ~1.1–1.75 km below ~50 km and ~3.5 km above ~50 km. Sassi et al. (2013) gives a detailed description of SD-WACCM-X.

The passive microwave limb sounder Sub-Millimeter Radiometer (SMR) on board the ODIN satellite also provides global measurements of the NO VMR for the winter periods considered in this study. However, the



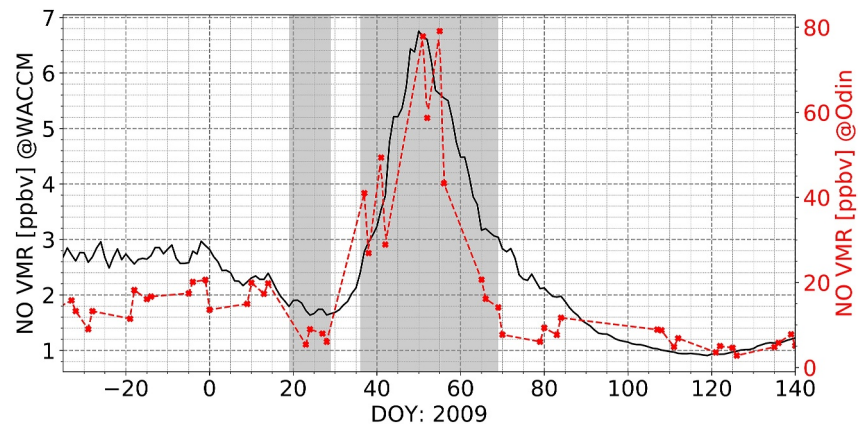


**Figure 2.** NO development over time during winter 2009 averaged between 65 and 75 km and zonal mean for latitude range 60–80°N. The gray shaded areas mark the approximate SSW- period (19–29 DOY) and the ES-period (36–69 DOY) in the winter 2009.

spatial and temporal resolution (~5 days) are unsuitable for analyzing the SSW/ES events along the VLF path of NRK-NYA. Still, the data help validate the NO simulations' qualitative behavior from SD-WACCM-X. For instance, Figure 2 shows the temporal evolution of NO retrieved from SD-WACCM-X simulations (black) and SMR-ODIN measurements (red) during the SSW/ES event in winter 2009. For both, a similar variation during the SSW/ES event is notable, characterized by a slight decrease during the SSW (around DOY 20) and a significant increase during the ES (with a peak around DOY 50). It is striking that the observed ODIN values are larger by a factor of 10–15 than the SD-WACCM-X values, with the largest deviations before the SSW period from –30 to +10 DOY 2009. Sinnhuber et al. (2024) compared NO data retrieved by different models and observations. They found that the polar winter NO value retrieved by WACCM-X is significantly underestimated in the thermosphere, which may be due to the fact that wave-induced transport is inadequately represented by the current gravity wave (GW) parameter scheme. An increase of the NO level in the winter mesosphere could be obtained with high-resolution WACCM-X simulations resolving GWs (Liu, 2025). Smith-Johnsen et al. (2022) also mention an underestimation of NO in wintertime in WACCM model runs due to an insufficient captured vertical transport. They improved the modeled NO transport by reducing the amplitude of the non-orographic GW and increasing the eddy diffusion.

Though the magnitudes of the NO concentration differ strongly, they agree in the temporal development. Since NO simulations from SD-WACCM-X can represent the general variability appropriately and due to their high spatial and temporal resolution, we use NO simulations from SD-WACCM-X in this study. However, the WACCM-X NO need to be treated carefully, as the GW parametrization might cause severe differences from observations (Liu, 2025). For our studies, we use the daily NO output data up to ~90 km, averaged along the pathway from the transmitter NRK to the receiver NYA. Like the MLS data, we used SD-WACCM-X grid points closest to the VLF signal propagation path (see Figure 1, blue triangles).

### 3. Results

#### 3.1. SSW and ES Events

To elaborate on the most likely impact of the SSW/ES events, we only considered SSW/ES events during solar minimum conditions in this study. The link NRK-NYA has data coverage from 2006, though continuous coverage occurs from 2008. We analyzed data until 2022, focusing on SSW/ES events during solar minimum conditions. During that period, several SSW/ES events could be identified, from which the events in the winters of 2009, 2010, 2018, and 2019 occurred during solar minimum conditions. We define the winter period as the beginning of November to the start of May. Due to increased solar activity, we excluded the SSW/ES events in 2012 and 2013. Moreover, the major warming event in 2021 was not considered, as there was no consecutive ES event. Thus, our analysis considers the SSW/ES events in the winters of 2009, 2010, 2018, and 2019. Figures 3a–3d show the temporal development of the temperature and Figures 4a–4d show the temporal development of the zonal wind for the single events. The temperature and zonal wind were averaged along the pathway (cf. Figure 1). All four

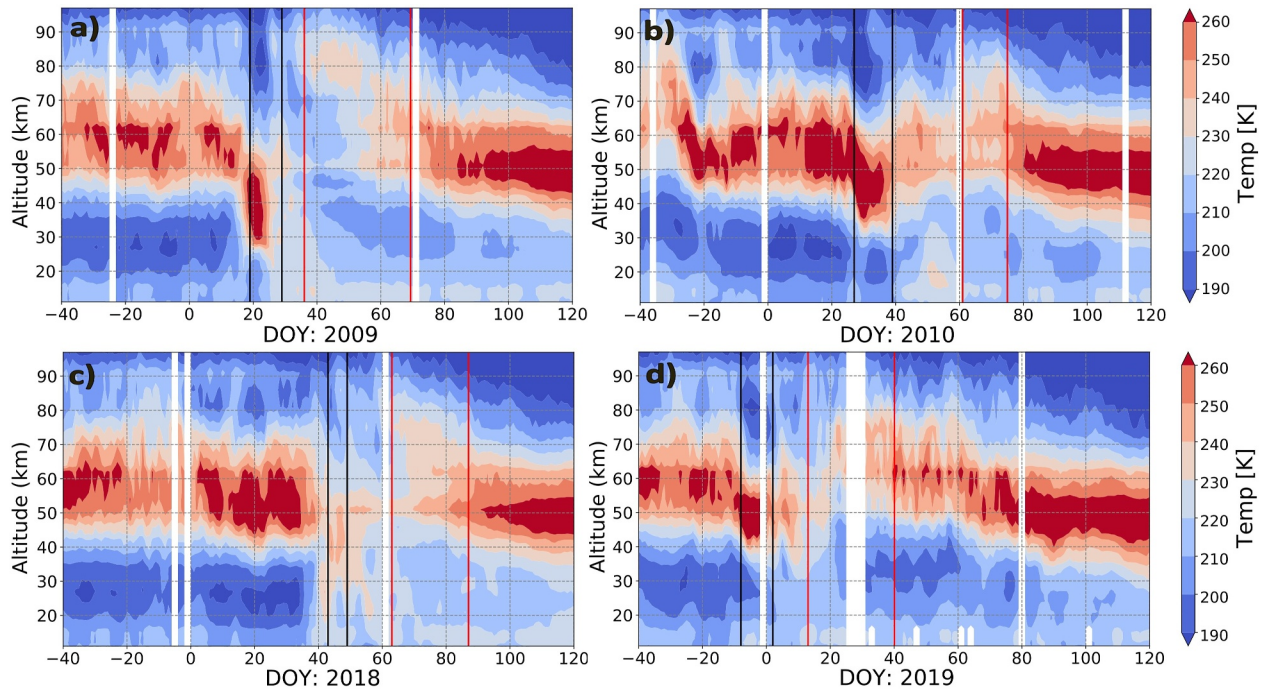


**Figure 3.** Temporal development over altitude of the temperature along the pathway NRK-NYA with identified start and end of SSW event (black vertical lines) and ES event (red vertical lines) in the mesosphere during the winters of 2009 (a), 2010 (b), 2018 (c) and 2019 (d). The determination of the start and end of the SSW and ES event is described in detail in Sections 3.2 and 3.3. Temperatures were obtained from the MLS observations.

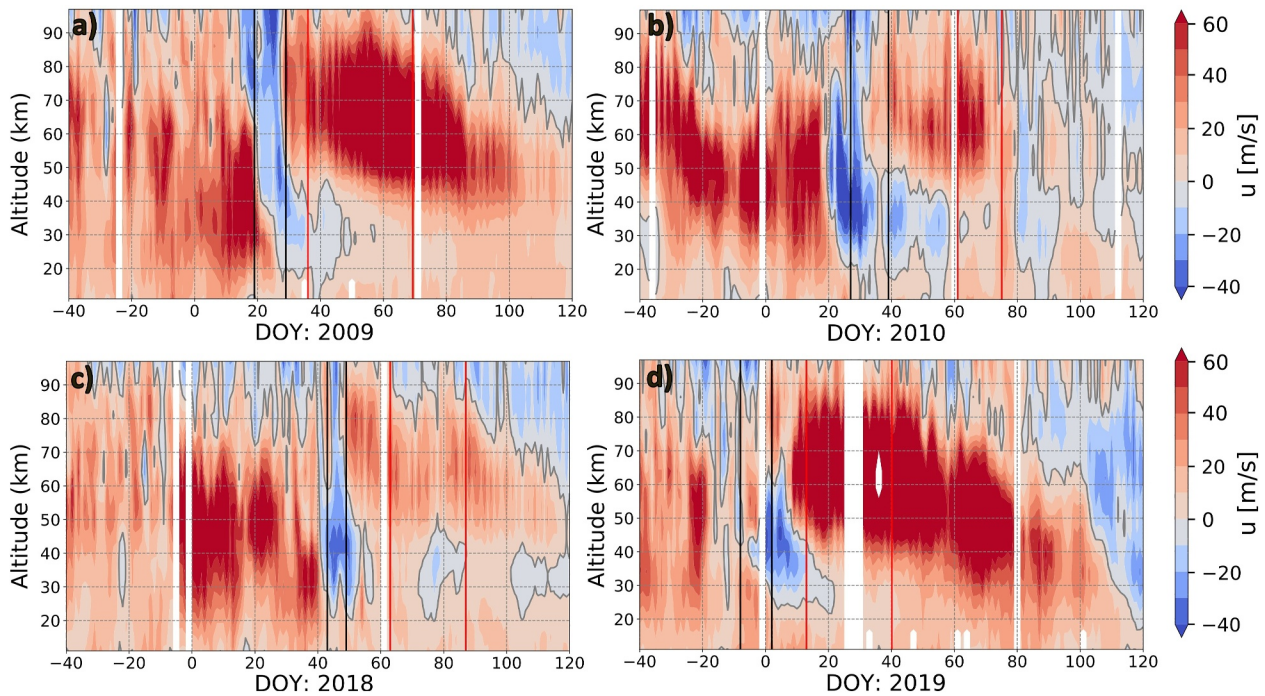


**Figure 4.** Temporal development over altitude of the zonal wind along the pathway NRK-NYA with identified start and end of SSW event (black vertical lines) and ES event (red vertical lines) in the mesosphere during the winters of 2009 (a), 2010 (b), 2018 (c) and 2019 (d). The determination of the start and end of the SSW and ES event is described in detail in Sections 3.2 and 3.3. The zonal wind was computed using MLS observations.

events show the aforementioned characteristic temperature and zonal wind modifications associated with major SSW and ES events (cf. Section 1), though they differ in development over time and altitude. The event in 2009 shows a clear structure with a descending stratopause and a cooling in the mesosphere during the SSW around DOY 20, a subsequent vanishing of the stratopause, and a reformation at higher altitudes, forming the elevated stratopause around DOY 40. The zonal wind reversal during the 2009 event starts some days earlier at altitudes higher than 75 km and then occurs over all altitudes down to approximately 25 km (Figure 4a). This clear structure cannot always be observed. In the event of 2019, the descending stratopause can be recognized to some extent (Figure 3d). However, the zonal wind reversal does not occur at any time at all altitudes since eastward (positive) wind patches disrupt it. In addition, the events differ in the time of occurrence. For example, the SSW/ES events in the winters of 2009 and 2010 occurred in mid-winter around 20–30 DOY (Figures 3a and 3b), the SSW/ES event in 2018 occurred relatively late in winter around 45–55 DOY (Figure 3c), while the SSW/ES event in 2019 started quiet early in end of December 2018 (Figure 3d). The different times of occurrence may affect the characteristics (e.g., strength and duration) of the SSW/ES events.

### 3.2. Mesospheric Onset Day of a SSW Event (MOD-SSW)

As individual SSW/ES events do not occur at the same times, the events are centered on the onset day of each event, for better comparability. Usually, the onset day of an SSW event is determined by specific zonal wind and temperature conditions at stratospheric heights around 10 hPa (Charlton & Polvani, 2007). However, the focus here is more on changes occurring in the mesosphere during SSW/ES events, as the VLF signal is reflected in mesospheric altitude ranges (60–90 km). Consequently, we want to center the events on the day the SSW events start in the mesosphere. The temporal and altitudinal development of the wind reversal and the characteristic changes in the temperature differ between the single events. Thus, considering the mesospheric altitude range for identifying the start of an SSW event in the mesosphere might be more appropriate than defining the onset day at a specific altitude as it is done for the stratosphere with 10 hPa. Since there is no definition for the onset day of an SSW event in the mesosphere, we developed an approach for systematically determining the Mesospheric Onset Day (MOD-SSW).

To identify the MOD-SSW, the wind reversal in the mesosphere, the characteristic temperature increase in the stratosphere, and the temperature decrease in the mesosphere are considered. Here, three parameters are used: the zonal wind, the standardized zonal wind described in Equation 1, and the standardized difference of the temperature at 40 km and at 70 km, given by Equation 3 with Equation 2. We chose 40 km to consider the warming in the stratosphere since the warming down to 30 km is delayed and not very pronounced in some SSW events. To detect the cooling, we chose 70 km, as the cooling is more pronounced here than at altitudes below 70 km, and the temperature is less variable than in altitudes above 80 km due to GW-wave interactions.

$$u_{\text{std}} = \frac{u - \bar{u}}{\text{std}(u)} \quad (1)$$

With  $\bar{u}$  as the average of the zonal wind over the years and  $\text{std}(u)$  as the standard deviation over the years representing the climatology of the zonal wind and its standard deviation, determined by the years from 2008 to 2023.

$$\Delta T_{\text{SSW}} = T(40\text{km}) - T(70\text{km}) \quad (2)$$

$$\Delta T_{\text{SSW}_{\text{std}}} = \frac{\Delta T_{\text{SSW}} - \overline{\Delta T_{\text{SSW}}}}{\text{std}(\Delta T_{\text{SSW}})} \quad (3)$$

With  $\overline{\Delta T_{\text{SSW}}}$  as the average of the difference of the temperature at 40 and 70 km over the years representing the climatology of the temperature difference and  $\text{std}(\Delta T_{\text{SSW}})$  as its standard deviation, determined by the years from 2008 to 2023.

Firstly, the zonal mean MOD-SSW is determined, for which the zonal average between 60 – 80 ° N of  $u_{\text{std}}$  and  $\Delta T_{\text{SSW}_{\text{std}}}$  is taken into account. The zonal mean MOD-SSW is defined on the first day of the period from November to May of each considered year, when  $\Delta T_{\text{SSW}_{\text{std}}} \geq 1$ ,  $u[60 : 80 \text{ km}]_{\text{std}} \leq -0.8$  and  $u[60 : 80 \text{ km}] < 0$  m/s are fulfilled. The altitude range specification in the bracket means the conditions must be fulfilled somewhere between 60 and 80 km.



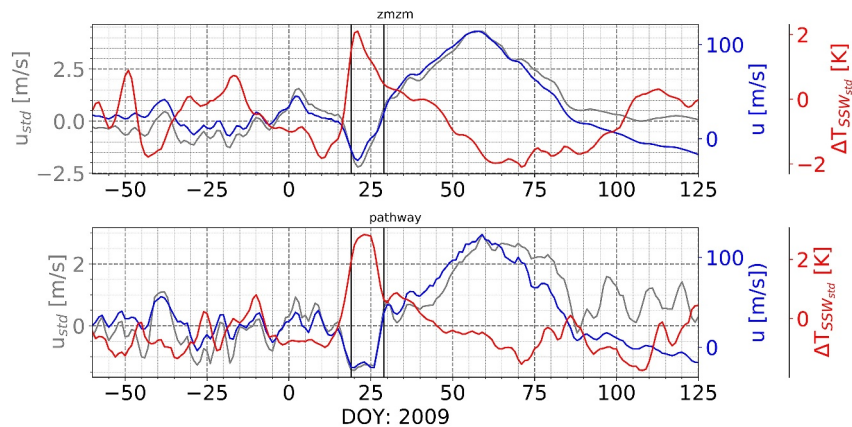


**Figure 5.** MOD-SSW definition shown for 70 km for the SSW/ES event in the winter of 2009 (top: zonal mean MOD-SSW, bottom: local MOD-SSW). The vertical lines mark the identified start and end of the SSW event at mesospheric altitudes.

Then the local MOD-SSW is determined, for which the average along the path from NRK to NYA is taken into account. The local MOD-SSW is defined on the first day of the period from November to May of each considered year, when  $\Delta T_{SSW_{std}} \geq 1$ ,  $u[60 : 80 \text{ km}]_{std} \leq -1$  and  $u[60 : 80 \text{ km}] < 0 \text{ m/s}$  are fulfilled. Note that the conditions regarding the zonal wind needed to be met in an altitude range and not at a certain altitude due to the diversity of SSW events (see Figure 4). The specific thresholds for determining the zonal mean MOD-SSW and the local MOD-SSW were chosen because they allowed us to detect all SSW events correctly, even those close to the spring transition. All days from November to May are determined by which the zonal mean MOD-SSW and the local MOD-SSW match. The final MOD-SSW is given by either one matching day or the first day of consecutive matching days. Note that, it is also possible to detect multiple MOD-SSWs. However, only one MOD-SSW per winter period was detected for the events considered here. The comparison with the zonal mean MOD-SSW is necessary to prevent short-term local fluctuations caused by waves, for example, from being incorrectly identified as the final MOD-SSW. Figure 5 uses the example of the SSW/ES event in the winter of 2009 to show how the MOD-SSW is determined.

### 3.3. Mesospheric Onset Day of an ES Event (MOD-ES)

As ES events are characterized by the disappearance of the stratopause and its subsequent re-formation at higher altitudes, a cooling in the stratosphere and a warming in the mesosphere can be observed. In addition, the polar vortex weakened during the SSW event and re-formed at mesospheric heights, manifested by strong eastward (positive) zonal winds at 60–80 km altitudes. ES events often show a longitudinal structure, likely determined by zonally asymmetric gravity wave drag (Okui et al., 2021). Thus, only local parameters (averaged along the pathway) are considered to identify the MOD-ES. The equations for the MOD-ES definition are similar to those for the MOD-SSW definition in Section 3.2. The start of an ES event is defined by the first day after the MOD-SSW, when the conditions  $u[70 : 80 \text{ km}]_{std} \geq 0.5$ ,  $u[70 : 80 \text{ km}] > 20 \text{ m/s}$ ,  $T[70 : 80 \text{ km}]_{std} \geq 0.8$  and  $\Delta T_{ES_{std}} \leq -1$ , with  $\Delta T_{ES} = T(65\text{km}) - T(80\text{km})$  are fulfilled. The difference in temperature at altitudes of 65 and 80 km turned out to be appropriate for identifying the increased temperatures that characterized the ES event. The specific thresholds for the MOD-ES determination were chosen to determine the ES events while neglecting short-term temperature variability likely due to enhanced GW interactions in this altitude range (Fritts & Alexander, 2003). The standardization of  $\Delta T_{ES}$  is computed as in Equation 3.

### 3.4. Characteristics of the SSW and ES Events

The MOD-SSW and MOD-ES for all here considered SSW/ES events were determined by the definitions described in Sections 3.2 and 3.3. The duration of the SSW event in the mesosphere is computed by the number of consecutive days from the MOD-SSW, until the following conditions are fulfilled:  $\Delta T_{SSW_{std}} < 1$  and  $u[60 : 80 \text{ km}] \geq 0 \text{ m/s}$ . The end of the ES event is calculated with the first day after the MOD-ES if  $\Delta T_{ES_{std}} \geq 0$



**Table 1**  
*Mesospheric Characteristics of SSW/ES Events Considered in This Study*

Year	MOD-SSW	Duration SSW	MOD-ES	Duration ES
	DOY	Days	DOY	Days
2009	19	10	36	33
2010	27	12	61	14
2018	43	6	63	24
2019	-8	10	13	27

and  $20 \text{ m/s} < u[70 : 80 \text{ km}] < 50 \text{ m/s}$ . The zonal wind restriction with lower and upper boundary was necessary to ensure that the end of an ES event is not determined too late since, in some cases, the zonal wind remains very strong even when the stratopause is no longer elevated. The characteristics of the single events are shown in Table 1. On average, an SSW event lasts approximately 10 days. The duration of an ES event varies between 14 days minimum and 33 days maximum. The time intervals between MOD-SSW and MOD-ES also differ from 17 days minimum to 34 days maximum. For the following explanations, we define the approximate SSW period as 0–10 days after MOD-SSW and the ES period as 25–50 days after MOD-SSW.

### 3.5. VLF Signal Amplitude Variation During Four SSW/ES Events

In the following, the temporal development of the VLF signal amplitude, atmospheric, solar, and geomagnetic parameters, mainly related to the VLF signal amplitude variation, are compared for the SSW/ES during the winter periods 2009, 2010, 2018, and 2019. The time series were centered on the MOD-SSW shown in Table 1 for better comparability.

The zonal wind and temperature are considered to investigate the impact of SSW/ES events on the VLF signal amplitude, as significant changes in these parameters characterize the SSW/ES events. Since vertical mass transport is also modified during SSW/ES events, changes in the concentration of the neutral components are expected. Here, we consider the minor constituents water vapor ( $\text{H}_2\text{O}$ ), ozone ( $\text{O}_3$ ), and nitric oxide ( $\text{NO}$ ), as they are known to influence the D-region ionization. Water vapor and ozone support electron loss, whereas nitric oxide supports electron production as it is photoionized by Lyman- $\alpha$  radiation (Mitra, 1978). Temperature,  $\text{H}_2\text{O}$ , and  $\text{O}_3$  were directly retrieved from Aura MLS, the zonal wind is the zonal component of the geostrophic wind computed by the geopotential height also retrieved by Aura MLS. SD-WACCM-X provides simulations of the NO data presented here. All data were averaged along the pathway from the Tx-Rx link NRK-NYA (cf. Section 2).

Figure 6 shows the temporal development of the daytime VLF signal amplitude during the SSW/ES event in 2009 (in green), 2010 (in blue), 2018 (in black), and 2019 (in red), each centered at the MOD-SSW (Table 1). The daytime VLF signal amplitude was computed by the daily average within the 11–13 LT range. In addition, the daytime VLF signal amplitude was smoothed with the Savitzky Golay filter (window size: 15, order: 3) for better legibility of the VLF signal amplitude variation (Luo et al., 2005). The temporal evolution of the VLF signal amplitude for the SSW/ES events in 2009, 2010, and 2018 shows a similar behavior (green, blue, and black lines in Figure 6). Around the MOD-SSW, the amplitude increases until it reaches a peak 7–10 days after the MOD-SSW, where the amplitude is enhanced by  $\sim 6$  dB. Subsequently, the amplitude decreases. Around 40 days after

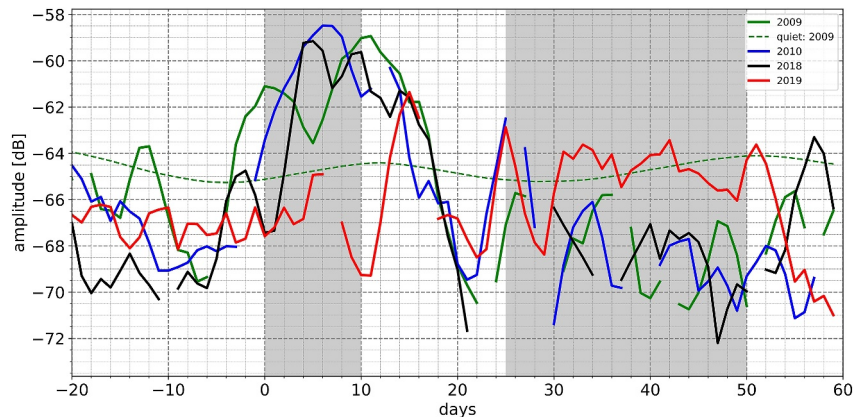


**Figure 6.** Temporal development of the daytime VLF signal amplitude for the SSW/ES events in the winters of 2009, 2010, 2018, and 2019, centered at the MOD-SSW listed in Table 1. The gray shaded areas mark the approximate SSW period (0–10 days) and the ES period (25–50 days). The green dashed line represents the quiet time line centered at the MOD-SSW 2009.

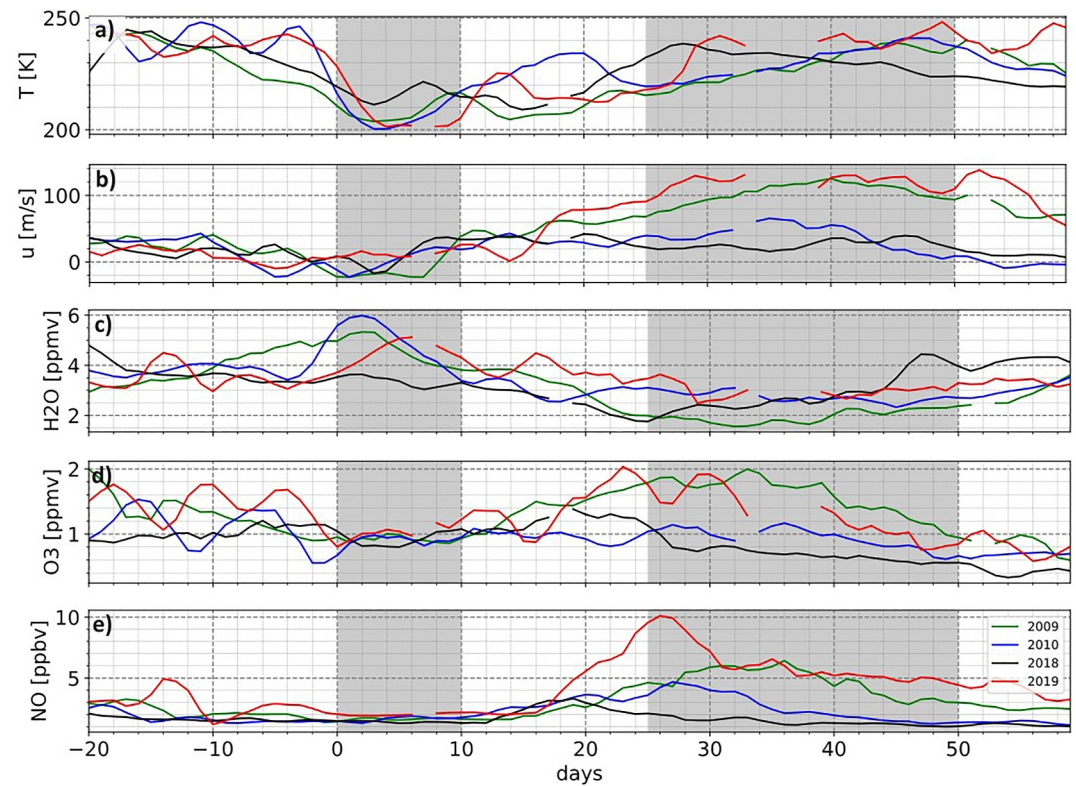


**Figure 7.** Development over time of temperature (a) and zonal wind (b), the volume mixing ratios of the minor constituents water vapor (c), ozone (d) and nitric oxide (e) at 70 km during four SSW/ES events, centered at the MOD-SSW listed in Table 1. The gray shaded areas mark the approximate SSW period (0–10 days) and the ES period (25–50 days).

the MOD-SSW, it reaches lower amplitude values ( $\sim\Delta 2$  dB) than before the MOD-SSW. To better recognize the disturbances during the SSW/ES 2009, the quiet time line centered at the MOD-SSW 2009 is also presented (green, dashed line). The quiet time line represents the seasonal VLF signal amplitude variation under undisturbed (solar, geomagnetic, atmospheric) conditions. It is computed by the composite of all years during that period (MOD-20 days to MOD + 60 days), by the same procedure as the seasonal variation is deducted described in Schneider et al. (2024). For better visibility, only the quiet time line centered at the MOD-SSW 2009 is presented in Figure 6, as an example. Supporting Information S1 shows the VLF signal variation during 2010, 2018, and 2019 and their quiet time lines. For the SSW/ES event in winter 2019, the VLF signal amplitude variation looks different (red line). It does not show a significant increase starting from the MOD-SSW. Around 15 days after the MOD-SSW, a slight increase of about 4 dB is notable, not followed by a pronounced decrease afterward, as observed during the other three events.

Figure 7 shows from top to bottom the temporal development of the temperature (Figure 7a), the zonal wind (Figure 7b), H<sub>2</sub>O (Figure 7c), O<sub>3</sub> (Figure 7d) and NO (Figure 7e) during the SSW/ES event in 2009 (in green), 2010 (in blue), 2018 (in black) and 2019 (in red), each centered at the MOD-SSW (Table 1). The study of the temporal development of the temperature at 70 km altitude, as depicted in Figure 7a, reveals a consistent pattern. For all events, the temperature experiences a significant decrease by 30–40 K from the MOD-SSW due to the mesospheric cooling during the SSW. A slow, steady temperature increase follows this decrease until the previous level is reached around 30–40 days after the MOD-SSW. The increased temperatures during the ES are more pronounced at altitudes above 70 km (not shown). Figure 7b shows the evolution over time of the zonal wind at 70 km. All events between 20 and 10 days before the MOD-SSW (–20 to –10 days) show moderate eastward (positive) zonal wind velocities between 5 and 40 m/s. Then, the zonal wind related to the events during the winter in 2010 (in blue) and 2019 (in red) turns westward (negative) around 6–4 days before the MOD-SSW. Between 0 and 10 days from the MOD-SSW, the zonal wind for the events in 2009, 2010, and 2018 became westward, which is associated with the wind reversal during the SSW. Here, the event in 2009 shows the longest period of

the wind reversal. Unlike the other three events, the zonal wind at 70 km altitude during winter 2019 already becomes westward 5 days before the MOD-SSW. It is eastward with low velocities between 0 and 20 m/s during the SSW period. An explanation for the eastward wind during the SSW period can be found by a closer look at the temporal and altitudinal development of the zonal wind in 2019 (Figure 4d). It shows that the westward wind occurs at 30–40 km altitudes, is disturbed by eastward wind from 50 to 75 km, and is westward again above ~ 75 km during the SSW period. Perturbations by atmospheric waves can be the reason for this inconsistent wind reversal. For all events, a strong increase of eastward zonal wind associated with the ES is observed from day 20 of the MOD-SSW, lasting at least 25 days, with the strongest eastward wind velocities during the events in 2009 and 2019.

In 2009 and 2010, the water vapor VMR evolution over time at 70 km altitude increases a couple of days before the MOD-SSW until it reaches the peak (+ $\Delta 2$  ppmv) around 2 days after the MOD-SSW (see Figure 7c). In 2019, the increase of the water vapor VMR at 70 km starts with the MOD-SSW and peaks around 7 days later. Subsequently, the water vapor VMR decreases until it reaches lower values than before the MOD-SSW (around +30 days from MOD-SSW,  $\sim \Delta 0.5 - 1$  ppmv). However, during the winter of 2018, no significant increase around the MOD-SSW can be recognized. Here, we should consider the late occurrence of the SSW/ES event in winter 2018 (SSW: 43 DOY, ES: 63 DOY), which is quite close to the spring transition. The climatology of water vapor at 70 km shows a decrease in the concentration during spring before it increases in summer (not shown). Removing the climatology from the water vapor in winter 2018, reveals a positive anomaly around the SSW period and a negative anomaly during the ES-period (not shown). This is an indicator, that during the SSW/ES event in 2018 the same vertical transport processes occur as during the other three here considered events. The water vapor climatology, the temporal and height development during the SSW/ES 2018, and the anomaly are shown in Supporting Information S1. Figure 7d shows the ozone VMR evolution at 70 km altitude for all four events, which decreases to 0.8–1 ppmv during the SSW period (shaded area). Before the MOD-SSW, the ozone concentration showed high variability and was enhanced by up to 2 ppmv for 2009, 2010, and 2019. The ozone VMR increases after the SSW period. The ozone variations of 2009 and 2019 show the most substantial increase up to 2 ppmv during the ES period. Similar to the ozone variation, the NO variation in Figure 7e shows a low NO VMR for all four events during the SSW period. It subsequently increases until it reaches maximum values during the ES period. The maximum values differ strongly between the events, with lowest values of 3 ppbv in 2018 and maximum values of 10 ppbv in 2019. The significant increase of the NO concentration during the ES period in 2019 agrees with ODIN measurements (not shown) and is also described in Pérot and Orsolini (2021). Striking is the enhanced NO VMR up to 5 ppbv around 20–10 days before the MOD-SSW in 2019, which can be related to the enhanced wave activity or also to solar or geomagnetic disturbances, as energetic particle precipitation is the primary source of nitric oxides ( $\text{NO}_x = \text{N}, \text{NO}, \text{NO}_2$ ) above the middle stratosphere at high latitudes (Jia et al., 2024). Note, that during the winter 2010 and 2019 the temperature, the zonal wind, the water vapor and the ozone concentration show a wave signature, which is particularly pronounced in 2019.

### 3.6. Solar and Geomagnetic Activity

Solar and geomagnetic disturbances are significant drivers of VLF signal amplitude perturbations (Nwankwo et al., 2022). Thus, it is necessary to consider the solar and geomagnetic activity during the four SSW/ES events to gain an overview of possible drivers responsible for the observed VLF signal amplitude variation. Figure 8 shows for all four events daily averaged Kp (a), Ap (b), DST (c) and the Auroral Electrojet (AE) Index (d) indices as proxies for geomagnetic disturbances, the F10.7 (e) and Lyman- $\alpha$  radiation (f) as indices for solar activity and the 10 MeV proton flux (g) as an index for EPP events, all provided from NASA/GSFC's OMNI data set (<https://omniweb.gsfc.nasa.gov/form/dx1.html>).

According to NOAA's Space Weather Prediction Center (SWPC), the F10.7 can vary from below 50 solar flux units (s.f.u.) to above 300 s.f.u. throughout a solar cycle (<https://www.swpc.noaa.gov/phenomena/f107-cm-radio-emissions>). Note that solar activity stays quite low during the winter of 2009, 2018, and 2019, with an F10.7 index of around 70 (Figure 8d). For the SSW/ES event 2010, the solar activity is slightly enhanced with a low/moderate F10.7 index between 80 and 90 sfu. The same conditions are shown in the Lyman- $\alpha$  radiation in Figure 8e, whereas there are slight enhancements of the Lyman- $\alpha$  radiation during the SSW/ES event 2010 between 20 and 10 days before the MOD-SSW, between 10–20 days and 40–50 days after the MOD-SSW. According to the 27-day moving average of the Lyman- $\alpha$  radiation over the last three solar cycles, we define a moderate Lyman- $\alpha$  radiation flux  $> 0.007 \text{ Wm}^{-2}$ . This threshold for a moderate Lyman- $\alpha$  radiation flux was not reached during the



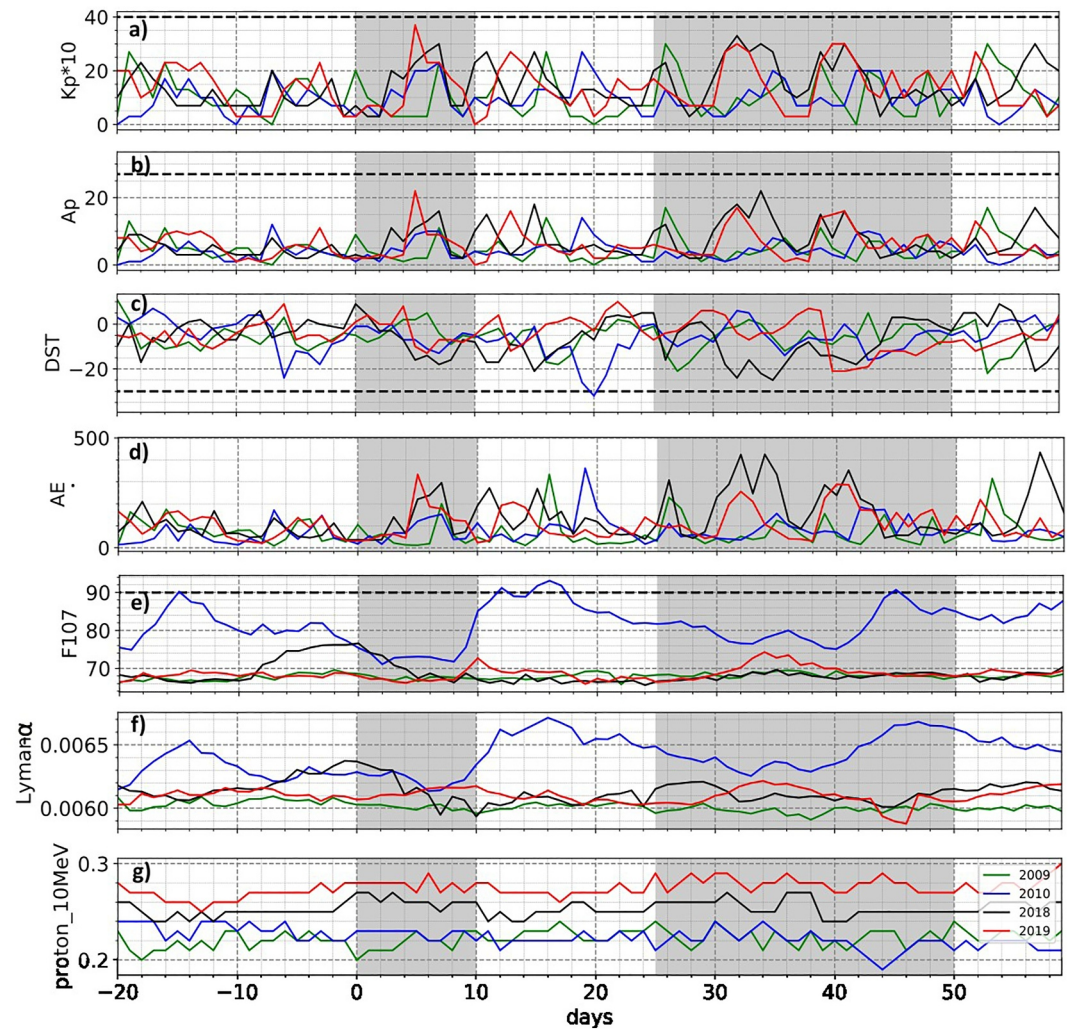


**Figure 8.** Development over time of the Kp index (a), Ap index in nT (b), DST index in nT (c), AE index in nT (d), solar radio flux at 10.7 cm (2,800 MHz) also called F10.7 index in solar flux units [sfu] (e), Lyman- $\alpha$  flux in  $W \cdot m^{-2}$  (f) and 10 MeV proton flux in  $cm^{-2} \cdot s^{-1} \cdot sr^{-1}$  (g) during four SSW/ES events (2009 in green, 2010 in blue, 2018 in black, 2019 in red), centered at the MOD-SSW listed in Table 1. The horizontal dashed lines represents upper quiet time thresholds. The gray shaded areas mark the approximate SSW period (0–10 days) and the ES period (25–50 days).

here-considered SSW/ES events. Furthermore, the F10.7 index and the Lyman- $\alpha$  radiation show oscillating variations during all events, likely with the 27-day solar cycle as the origin. The 10 MeV solar proton flux for all four events looks inconspicuous. The proton flux during the SSW/ES period in winter 2019 has the highest level compared to the other three events. However, the proton flux for all four events is far below the SWPC 10 MeV Warning Threshold. A weak storm is categorized with  $-30 \text{ nT} > \text{Dst} > -50 \text{ nT}$ ,  $K_p > 4$  and  $a_p > 27$  (cf. Table 1 of Loewe & Prölss, 1997). An Auroral Electrojet peak  $500 \text{ nT} < \text{AE} < 1000 \text{ nT}$  is associated with a moderate storm or substorm (Gulyaeva, 2017). Those thresholds were reached around 45 days before the MOD-SSW in 2019 with  $K_p \sim 4$ ,  $a_p \sim 30$  and  $\text{DST} \sim -35 \text{ nT}$ . Though the AE index is also increased around 50–45 days before the MOD-SSW in 2019 ( $\sim 490 \text{ nT}$ ), it does not reach the threshold for a moderate storm. The extended time series of the discussed solar and geomagnetic parameters are shown in Supporting Information S1. Such weak geomagnetic storm can produce NO at thermospheric/upper mesospheric altitudes (Clilverd et al., 2009) which descends under strong polar vortex conditions (Solomon et al., 1982). Effects of solar and geomagnetic events on the atmosphere and the ionosphere can occur delayed. For instance, an enhancement of  $\text{NO}_x$  produced by energetic particles can be observed after the particle precipitation event has started and is far from the production area due to the long lifetime of  $\text{NO}_x$  in polar winter and its transportation by atmospheric winds (Rozanov et al., 2012; Sinnhuber

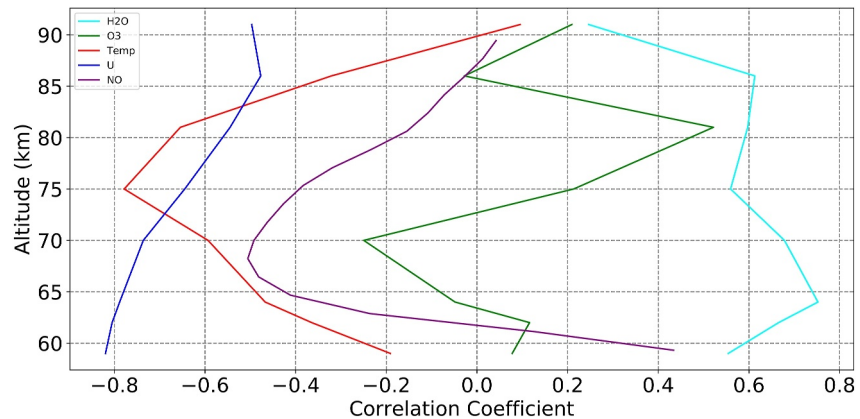


**Figure 9.** Variation of the correlation coefficient over altitude for certain atmospheric parameters.

et al., 2012). It is conceivable that the weak geomagnetic storm 45 days before MOD-SSW caused the NO enhancement in 70 km altitude observed 20 to 10 days before the MOD-SSW in 2019 (Figure 7e). Thus, solar and geomagnetic effects might overlap slightly the SSW/ES event 2019.

### 3.7. Average VLF Signal Amplitude Variation During SSW/ES Events

Looking at the single events in Figure 6, it is remarkable that the VLF signal amplitude of the three SSW/ES events in 2009, 2010, and 2018 show a very similar variation characterized by a significant increase during the SSW period, followed by a decrease during the ES period. However, the VLF signal amplitude variation during the SSW/ES event in winter 2019 differs from the other three events as it increased almost 2 weeks later than during the other three events and did not show a decrease during the ES period. In this section, the VLF signal amplitude variations and the most likely atmospheric drivers are averaged for the three SSW/ES events to get a clearer picture of the average impact of the SSW/ES event on the VLF signal amplitude under quiet sun conditions. We are aware that three events are too few for statistical statements. Still, the average gives an impression of the variations during SSW/ES events. A cross-correlation with the averaged VLF signal amplitude and the average of each parameter is computed for each altitude for the time frame  $-20$  to  $+60$  days from MOD-SSW, respectively, to evaluate the best altitude for further analysis. Figure 9 shows the height evolution of the correlation coefficient averaged for the time lag period  $-10$  to  $0$  days from 60 to 90 km, which is expected to be the reflection height range of the VLF signal. We chose the lag period  $-10$  to  $0$  days since we observe a delay of the VLF signal reaction to changes in the atmospheric parameters in cross-correlations of the time series (not shown). The values provide qualitative information regarding the altitude with the strongest correlations rather than quantitative information. Comparing the cross-correlation coefficients, the temperature at 75 km, the zonal wind at 60 km, and water vapor at 65 km show the highest correlations (temp:  $-0.76$ ,  $H_2O$ :  $+0.75$ , zonal wind:  $-0.8$ ) with the VLF signal amplitude. Between 65 and 70 km, NO reaches the highest correlation coefficients with  $-0.5$ , and at an altitude of 80 km, ozone reaches a maximum of  $+0.5$ . The here-determined altitudes for each parameter are used to analyze the temporal development of the VLF signal amplitude and the atmospheric parameters during the average SSW/ES event and the SSW/ES event in 2019. To understand the general processes during SSW/ES events that affect the VLF signal, it was more beneficial to average the three similar events and look at the altitudes with the highest correlations. However, a detailed analysis of the individual events could be carried out as a subsequent study focusing on the effect of the different temporal and vertical development and the strengths of the individual SSW/ES events on the VLF signal amplitude.

Figure 10 shows from top to bottom the temporal development of VLF signal amplitude, the temperature at 75 km, the zonal wind at 60 km, the water vapor VMR at  $\sim 65$  km, the ozone VMR at 80 km, and the NO VMR at 68 km. The solid lines represent the average of the events in 2009, 2010, and 2018, shaded with  $\pm 1$  standard deviation. The dashed lines represent the variation during the SSW/ES event 2019. The average amplitude variation of the VLF signal is characterized by a significant increase of about  $\Delta 8$  dB, which starts  $\sim 7$  days before the MOD-SSW (day 0), peaks around day 7–8 after the MOD-SSW and then drops to a lower level (about  $\Delta 2$ – $3$  dB lower) than before the MOD-SSW from day 30 onwards (Figure 10a). The VLF signal amplitude variation

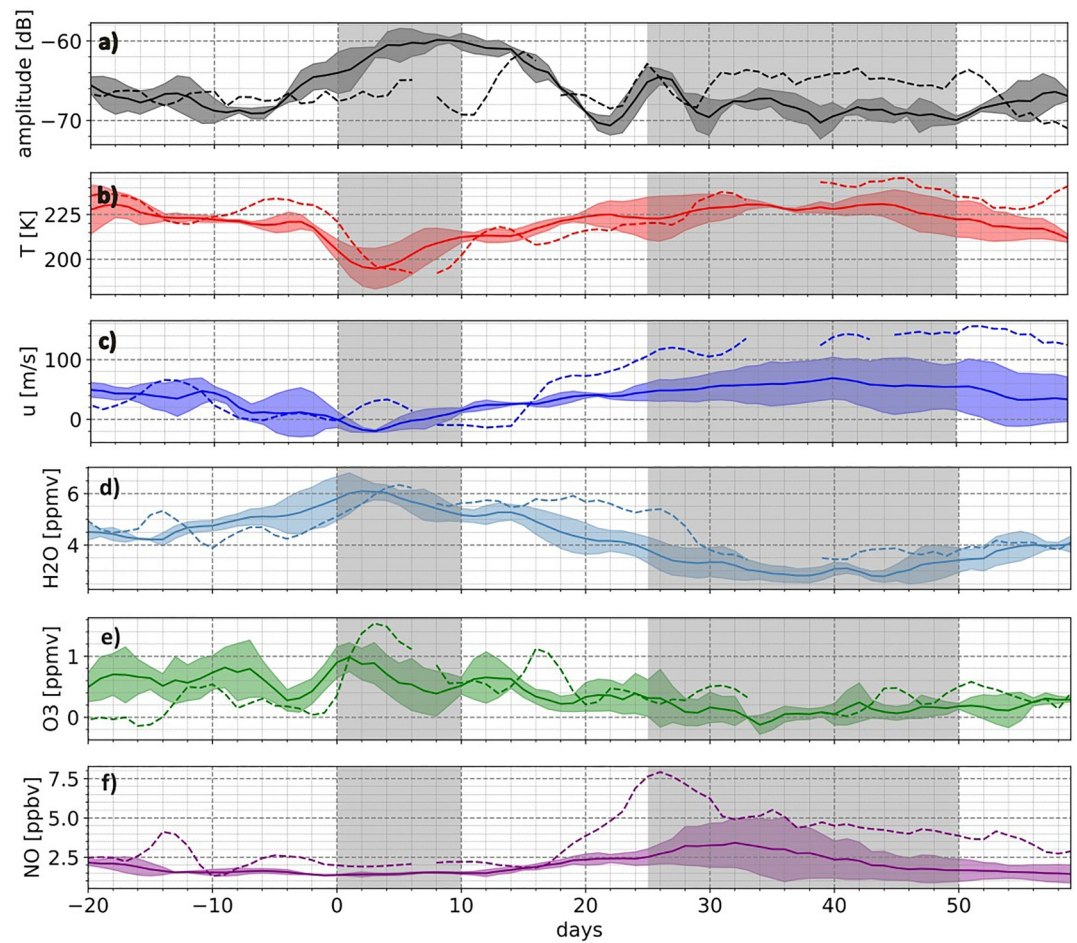


**Figure 10.** Development over time of daytime VLF signal amplitude in black (a), temperature at 70 km in red (b) and zonal wind at 60 km in dark blue (c) as well as the volume mixing ratios of the minor constituents water vapor at 65 km in bright blue (d), ozone at 80 km in green (e) and nitric oxide at 68 km in purple (f). The solid line represents the average of three SSW/ES events (2009, 2010, 2018) and the dashed line represent the SSW/ES event during winter 2019, all centered at the MOD-SSW listed in Table 1. The colored shaded areas span one standard deviation and the gray shaded areas mark the approximated SSW period (0–10 days) and the ES period (25–50 days).

for the SSW/ES event 2019, represented by the dashed line, does not show the increase/decrease during the SSW/ES period. There is no notable enhancement around the MOD-SSW. As observed in the average variation, the VLF signal amplitude during 2019 did not decrease to a lower level during the ES period. On the contrary, it increases and stays at an enhanced level of  $\Delta$  2–3 dB compared to the period before the MOD-SSW.

The average temperature at 75 km in Figure 10b decreases from  $\sim$ 1–2 days before the MOD-SSW. The cooling peak of approximately 20 K occurs about 2–3 days after the MOD-SSW, followed by a continuous rise in temperature with the highest values during the ES period (10 K higher than the values in the week before the MOD-SSW). The temperature variation for the SSW/ES event in the winter of 2019 shows temperatures up to  $\Delta$  10 K higher than the average a few days before the SSW period. Furthermore, the mesospheric cooling during the SSW period lasts about 2–3 days longer than the average. The averaged zonal wind in Figure 10c shows the characteristic wind reversal during an SSW event up to  $-20$  m/s a few days after the MOD-SSW and an enhanced eastward zonal wind up to  $\sim$ 60 m/s during the ES period. Be aware that, especially during the ES period, the standard deviation of the average zonal wind is quite large (approximately  $\pm$  30 m/s), caused by differences in the strength of the positive zonal wind enhancement between the four events. All the more striking is that the zonal wind variation during the SSW/ES event in 2019 shows strong eastward zonal wind up to 120–130 m/s during the ES period, which exceeds the averaged zonal wind by almost two standard deviations. Whereas the zonal wind in



the winter of 2019 during the SSW (~day 0) does not show an apparent reversal at the here-considered altitude of 60 km.

During the SSW period, the water vapor is increased with a maximum peak around day 2–4 after MOD-SSW (Figure 10d). Subsequently, it decreases until it reaches the lowest value during the ES period. In line with the average variation, water vapor during the SSW/ES event in the winter of 2019 also increases around the SSW. However, the enhanced water vapor concentration in the winter of 2019 lasted almost 2 weeks longer than the average water vapor variation. During the ES period, the water vapor variation in the winter of 2019 also decreased but did not reach such low values as in the average variation. Generally, the averaged ozone concentration at 80 km in Figure 10e is higher during the SSW period (peak value of ~1 ppmv around MOD-SSW) than during the ES period (0.1–0.2 ppmv). The ozone concentration at 80 km during the SSW period 2019 is about 0.6 ppmv higher than average. Though the general tendency of the ozone concentration is negative after the SSW period, there are frequent positive peaks with higher ozone concentration than the average (e.g., at 16–18, 30, or 44 days from MOD-SSW). Figure 10f shows the averaged NO variation and the NO variation for the SSW/ES event in 2019 at 68 km. The averaged NO variation shows consistently low values of 1.5–2 ppbv from 20 days before until 16 days after the MOD-SSW. After the SSW period, the NO concentration increases until it reaches the peak of 3 ppbv around 32 days after MOD-SSW. During almost the complete ES period, the NO concentration is enhanced with values above 2 ppbv. The enhancement of the NO concentration is caused by the downdraft, which accompanies the ES event and is thematized in various publications (e.g., Manney et al., 2009; Randall et al., 2009, and others). The centering at the MOD-SSW and the different periods between MOD-SSW and MOD-ES likely cause large standard deviations during the ES period. Note, the NO increase during the ES period 2019 is significantly stronger than in the averaged variation, with a peak value of about 7.5 ppbv. In contrast to the average, the NO concentration in 2019 is also enhanced 16 to 12 days before the MOD-SSW and reaches a peak of about 4 ppbv. The enhanced NO concentration may be linked to a geomagnetic storm around 45 days before MOD-SSW 2019 (cf. 3.6). The standard deviation shown in Figure 10 is calculated for the three events and is therefore not representative in statistical terms. However, it conveniently shows the spread of the events in the altitude under consideration. In addition, the standard deviation helps to estimate how much the VLF signal amplitude and the atmospheric parameters during SSW/ES 2019 deviate from the average of the other three events.

As mentioned in Section 3.5 there is a pronounced wave signature notable in the VLF signal variation as well as in almost all atmospheric parameters during the winter of 2019 leading to deviations from the average (e.g., temperature in Figure 10b or ozone in Figure 10e).

In summary, the average VLF signal variation of the SSW/ES events in 2009, 2010, and 2018 is characterized by an increase of the VLF signal amplitude during the SSW period, when the mesospheric temperature, zonal wind, and NO are decreased, and H<sub>2</sub>O is increased. The VLF signal amplitude is reduced during the ES period when the mesospheric temperature, zonal wind, and NO are increased, and H<sub>2</sub>O is decreased. The VLF signal variation during the SSW/ES event in 2019 differs from the average of the three events, as it shows only a short-term enhancement of the VLF signal amplitude at the end of the SSW period and does not show a decrease at all during the ES period. The atmospheric parameter variations during the SSW/ES event in 2019 were generally similar to the other three events. However, they showed higher variability and seemed disturbed by wave interactions. In addition, the solar and geomagnetic indices, which were primarily low, indicate a weak geomagnetic storm approximately 45 days before the MOD-SSW in 2019, likely causing overlapping effects.

## 4. Discussion

The presented results lead to two main questions. First, what general mechanism drives the characteristic VLF signal variation observed during the SSW/ES event in winter 2009, 2010, and 2018? Second, why does the VLF signal variation during the SSW/ES event in winter 2019 not show a similar signature? Both questions are discussed in the following.

### 4.1. Mechanism Causing Average VLF Signal Signature During Three SSW/ES Events

As described in the results section, the averaged VLF signal amplitude variation during the SSW/ES event in Figure 10a shows a clear signature characterized by an amplitude increase during the SSW period and a decrease during the ES period. Since the prevailing solar and geomagnetic conditions during the three SSW/ES events used

for the average were quiet (see Figure 8), it is assumed that the changes in the VLF signal amplitude leading to the here mentioned characteristic signature have an atmospheric origin. The good correlation coefficients for specific atmospheric parameters at certain altitudes and support this assumption. Especially temperature, zonal wind, and water vapor show a strong correlation of about  $|R| \sim 0.7\text{--}0.8$  (Figure 9). Be aware that a strong correlation does not necessarily mean a physical connection. However, combined with background knowledge, it can serve as an indicator. For instance, the correlation coefficient for the VLF signal and the NO is moderate ( $R \sim -0.5$ ). Still, it is known that NO influences the VLF signal as it is one of the primary ionization sources in the D-region. The averaged NO variation in Figure 10f shows a significant enhancement from day 25–30 after the MOD-SSW lasting over the entire ES period due to the often observed enhanced downdraft during an ES event (Chandran et al., 2014). This enhanced NO concentration impacts the ionization in mesospheric altitude regions (Clilverd et al., 2007b). Therefore, the NO is expected to affect the VLF signal not during the complete SSW/ES period but rather during the ES period, which might cause a moderate correlation coefficient. Computing the correlations for the time series centered at the MOD-ES increases the correlation coefficient for NO to  $-0.6$  (not shown). The high correlation coefficients for the temperature, zonal wind, and water vapor concentration indicate that those changes match and may have a direct or indirect connection.

The time series for the single events are centered on different days of the year and then averaged. Since the solar and geomagnetic parameters are not affected by the atmospheric changes associated with the SSW/ES period, a correlation with the average provides no physical information. Correlations for the single events were weak and inconsistent for the solar and geomagnetic parameters (not shown), which may have multiple reasons. First, we consider the weakly sun-lit winter period in the high latitudes. Direct ionization processes by Lyman- $\alpha$  radiation can only occur during a short time of the day, which can be one reason for the low correlation. Low correlations with Lyman- $\alpha$  fluxes and geomagnetic parameters are also found by Xu et al. (2024), where they suggest that solar Lyman- $\alpha$  fluxes and the geomagnetic indices are almost uncorrelated with the annual oscillation of VLF data in low and middle latitude region. It can be assumed that the correlation of the VLF signal and Lyman- $\alpha$  radiation will likely become stronger the longer the considered period (multiple solar cycles). Furthermore, we would expect an increasing correlation with the geomagnetic parameters by considering storm periods with direct effects in the D-region. The correlation of solar and geomagnetic parameters with the VLF signal during storm periods and quiet time exceeds the scope of this study. However, it is another interesting subject for further studies.

As we want to understand the mechanism that drives the VLF signal amplitude variation during an SSW/ES event, we need a general overview of the parameters that control the VLF signal. The Long Wavelength Propagation Capability (LWPC) code is a collection of separate programs enabling the simulation of the VLF signal propagation (Ferguson, 1998). LWPC provides the options to either vary the simplified controlling parameters in the shape of the sharpness (gradient) of the vertical electron density profile named  $\beta$  and effective reflection height  $h'$  (Wait & Spies, 1964) or to include the direct electron density profiles together with a vertical collision frequency. Combining the controlling parameters, sharpness and effective reflection height, with the observed changes in temperature, zonal wind, water vapor, and NO, the averaged VLF signal amplitude variation during an SSW/ES event might be explained by the following mechanism. As shown in Figures 10b and 10d, the mesospheric temperature decreases, and the water vapor concentration increases during the SSW period. According to Bajčetić et al. (2017) the recombination coefficient for the D-region is indirectly proportional to the square root of the temperature:

$$\alpha_{\text{eff}} \propto \left( \frac{T_e}{300} \right)^{-0.5} \quad (4)$$

With  $\alpha_{\text{eff}}$  as effective recombination coefficient and  $T_e$  as electron temperature which is assumed to be equal to the neutral temperature  $T_n$  due to thermal equilibrium in the D-region (Schmitter, 2011). Thus, a decrease in the temperature, as it occurs during an SSW in the mesosphere increases the recombination, which leads to electron loss. In addition, since water clusters have a high recombination rate (Kelleys, 2009), we can assume that an enhancement of the water vapor concentration in the mesosphere results in a decrease of the electron density. This indirect dependence of the electron density of the water vapor concentration was already mentioned in Mitra (1978) and could also be confirmed with the help of the Sodankylä Ion and Neutral Chemistry Model (SIC), a 1-dimensional coupled model of the chemistry of the middle atmosphere and the ionospheric D-region. A detailed description of the original SIC model can be found in Turunen et al. (1996) and Verronen et al. (2005).

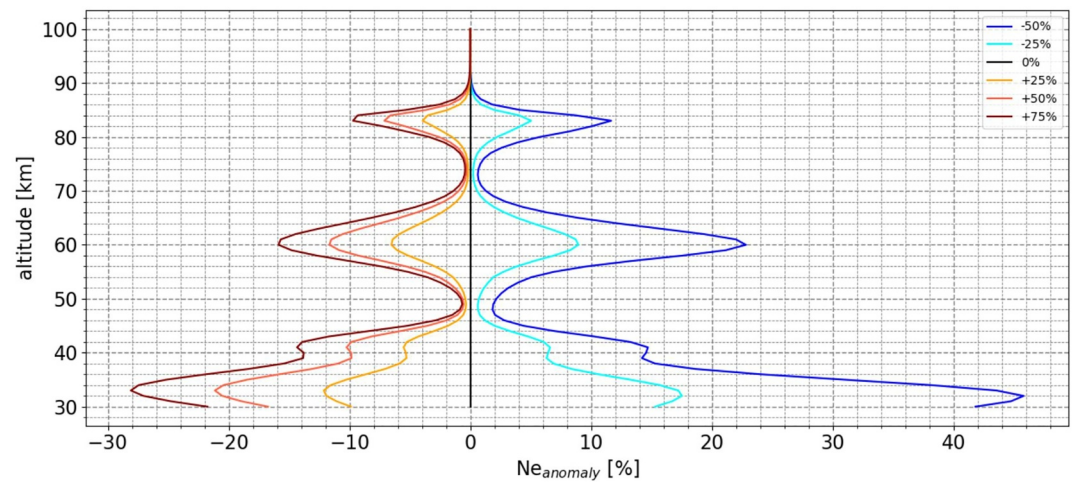


**Figure 11.** Sensitivity of the electron density to the water vapor for the midpoint position of the link NRK-NYA (72°N, 12°W) on 27 January 2009, from test simulations by the SIC model where the water vapor was manually increased/ decreased.

Figure 11 shows the sensitivity of the vertical electron density profile to water vapor from a set of test simulations by the SIC model where the water vapor concentration was manually increased/decreased. The test simulations reveal an indirect dependency between the water vapor concentration and the electron density. Note that the strength of the indirect dependency varies with altitude. It is particularly strong in the altitude regions from 30 to 40 km, from 55 to 65 km, and from 80 to 85 km. The last two altitude regions are especially interesting for us because they are located in the reflection height range of the VLF signal, which we assume is from 60 to 90 km. The 27 January 2009 was chosen for the test simulations since then the SSW has completely developed at midpoint positions of the NRK-NYA pathway. However, the SIC model does not simulate the SSW.

Moreover, the decrease in temperature influences the electron-neutral collision frequency. As it is stated in Thrane and Piggott (1966) and Vuthaluru et al. (2002), the collision frequency depends directly on the pressure. Vuthaluru et al. (2002) could find good agreements of the collision frequency with rocket measurements with the following equation

$$\nu(h) = 1.21 \cdot 10^8 \cdot p(h) \cdot s^{-1} \quad (5)$$

with  $p$  as pressure in dependency of the altitude  $h$ . Inserting the barometric formula for the pressure obtains:

$$\nu(h) = 1.21 \cdot 10^8 \cdot p_0 \cdot e^{\frac{-g \cdot M \cdot h}{R \cdot T(h)}} \cdot s^{-1} \quad (6)$$

With  $p_0$  for the reference pressure at sea level,  $g$  for the gravitational acceleration,  $M$  for the molar mass of Earth's air,  $R$  for the universal gas constant, and  $T$  for the temperature in dependency of the altitude  $h$ . Equation 6 concludes that the collision frequency in the D-region directly depends on the temperature.

The temperature decrease in the mesosphere during the SSW period leads to increased recombination, causing a reduction in the electron density below the so-called ledge region (~80–90 km). The electron density increases rapidly in the ledge region due to the absence of water cluster ions (Mitra, 1978) and the abrupt appearance of atomic oxygen (McCormick & Cohen, 2021). We assume that this change in the electron density profile during the SSW period increases the sharpness  $\beta$  at the reflection height of the VLF signal. However, it is not clear whether the reflection height also changes. In addition to that expected higher  $\beta$ , it is assumed that the absorption of the VLF signal decreases as the collision frequency decreases (Macotela et al., 2021). Opposing processes are to be expected during the ES period, where a temperature increase ( $\rightarrow$  decrease of recombination coefficient and increase of collision frequency) and a decrease of the water vapor concentration ( $\rightarrow$  decrease recombination coefficient), in addition to an enhanced NO concentration, lead to an increase in the electron density below the ledge region. Since the NO is drawn downward by the ES accompanied downwelling to low mesospheric/upper



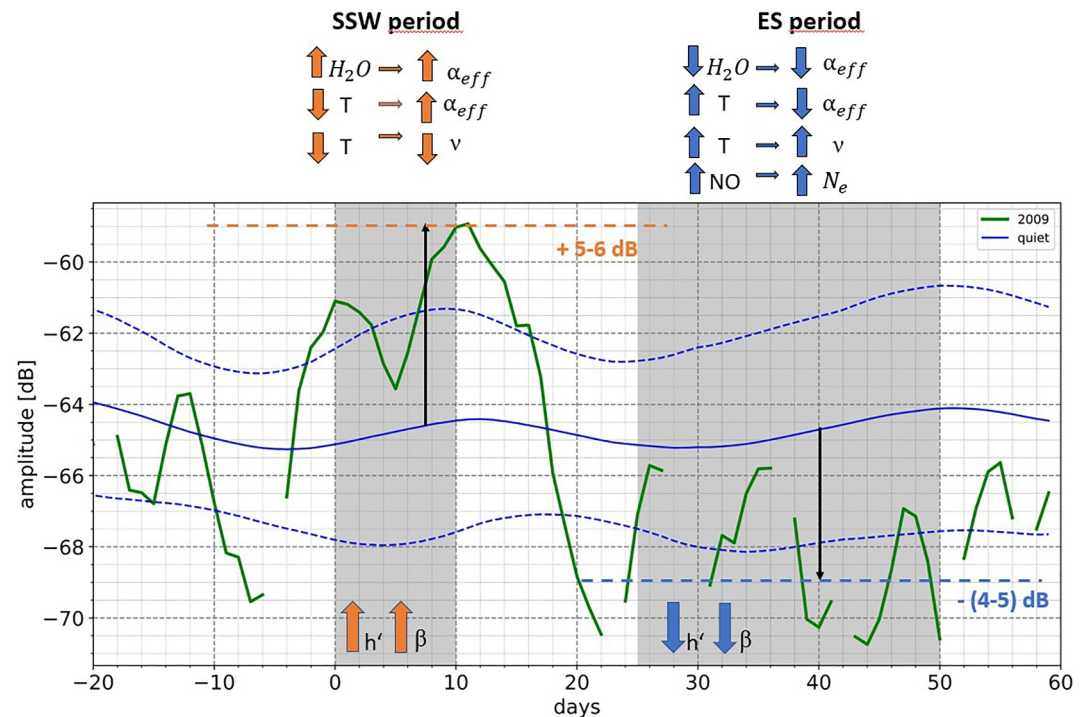


**Figure 12.** Scheme of the proposed mechanism, driving the average daytime VLF signal amplitude signature during SSW/ES events under quiet solar and geomagnetic conditions. The gray shaded areas mark the approximate SSW period (0–10 days) and the ES period (25–50 days). The dashed lines are  $\pm 1 \sigma$ .

stratospheric altitudes, the electron density increases at those altitudes. However, this results in a fading of the vertical profile and a lowering in the sharpness  $\beta$ . Moreover, it can be assumed that the effective reflection height of the VLF signal moves downwards. For instance, in Clilverd et al. (2006) simulations show that an increase of mesospheric NO by a factor of 100 would lead to the rise of the electron density by a factor of 10, which again results in a lowering of the ionospheric reflection height for VLF/LF waves by 10 km. The processes leading to the amplitude decrease during the ES period are similar to the physics of the winter anomaly, which is an increased radiowave absorption during winter. According to Danilov (1981), the increased absorption in winter results from an electron concentration increase in the D-region caused by the enhanced NO concentration and increased temperatures. Furthermore, a decrease in the VLF reflection height is observed during the winter anomaly (Belrose, 1967). Thus, the ES can be considered a strong winter anomaly.

In summary, especially the changes in the mesospheric temperature and the concentrations of the minor constituents  $H_2O$  and NO during an SSW/ES event are assumed to induce changes in the collision frequency, vertical gradient electron density profile and the reflection height of the VLF signal resulting in the observed VLF signal amplitude variation.

Note that this study discusses the variation of the daytime VLF signal amplitude. Since the D-region ionization varies between daytime and nighttime, the described processes in the suggested mechanism might deviate at different times of the day. This question exceeds the scope of this paper. However, it would be worthwhile to do further studies.

Figure 12 shows the assumed mechanism resulting in the averaged VLF signal amplitude variation during an SSW/ES event in quiet solar and geomagnetic conditions. Also shown in Figure 12 is the VLF daytime variation for the link NRK-NYA during the SSW/ES event in 2009 (in green), the quiet timeline for that period of the year (in blue), and the dashed lines are  $\pm$  one standard deviation to the quiet time line. The standard deviation refers to the average over all years VLF signal measurements were available (from 2008 to 2023 for the Tx-Rx link NRK-NYA). The VLF signal amplitude variation generally shows a high variability during wintertime due to the short illumination time and enhanced influence of atmospheric waves. This variability causes higher standard

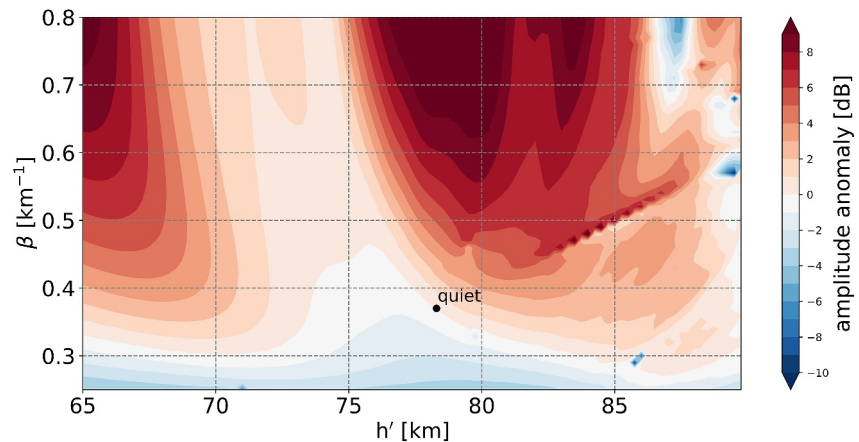


**Figure 13.** Amplitude anomalies in the LWPC parameter space, spanned by the sharpness of the vertical electron density profile  $\beta$  and the effective reflection height  $h'$ , determined for the link NRK-NYA. The black dot marks the pair  $\beta = 0.37$  and  $h' = 78.3$  km, used as reference for quiet daytime.

deviations than during summer. Still, the VLF signal amplitude perturbations in 2009 exceeded the high standard deviation. The assumed mechanism can be described as follows: During the SSW period, the increased  $\text{H}_2\text{O}$  concentration and the decreased temperatures enhance the recombination coefficient. Thus, electron loss occurs in the mesosphere, which causes a sharp edge of the vertical electron profile and an enhancement of the effective reflection height, increasing the VLF signal amplitude. The amplitude increase is amplified as the absorption is reduced by the decreased collision frequency due to the decreased temperatures. The opposite processes happen during the ES period, where the decreased  $\text{H}_2\text{O}$  concentration and the increased temperatures reduce the recombination coefficient and, thus, increase the electron density. In addition, NO is drawn downwards by downwelling during the ES period, causing an electron density enhancement at lower altitudes. By the enhancement of the electron density at upper stratospheric/lower mesospheric altitudes, the vertical electron density profile is more faded, and the effective reflection height decreases, resulting in a decrease of the VLF signal amplitude. Furthermore, the amplitude decrease is amplified as the absorption is enhanced by the increased collision frequency due to the increased temperatures. We examine the VLF signal amplitude variation during the SSW/ES event 2009 (green line in Figure 12) to evaluate the assumed mechanism. For the SSW/ES event in 2009, an amplitude increase during the SSW period by  $\sim 5\text{--}6$  dB and a decrease by  $\sim 4\text{--}5$  dB during the ES period is notable.

These amplitude anomalies can be used to identify the possible changes in the ionospheric parameter  $\beta$  and  $h'$ . For this purpose, the parameter space for the VLF wave propagation from NRK to NYA derived from LWPC is used. The parameter space assigns an amplitude for each  $\beta$  and  $h'$  combination. The amplitudes computed by LWPC are not normalized, and it is difficult to compare the observations with the simulations. Therefore, the amplitude anomaly resulting from the difference between the amplitude in the parameter space and the quiet day amplitude is considered. Ferguson (1998) defined  $\beta = 0.37$  and  $h' = 78.3$  km as a quiet, daytime ionospheric parameter for a 30 kHz signal in high latitudes, which matches quite well with the conditions of the link NRK-NYA. The quiet daytime amplitude is determined by the amplitude for this parameter combination ( $A_{\text{quiet}} = 60.8393$  dB) in the parameter space (not shown). Figure 13 shows the parameter space for the amplitude anomaly, computed by the subtraction of the quiet time amplitude of 60.8393 dB from the actual parameter space amplitudes. There is neither a linear dependency between the VLF signal amplitude anomaly and the parameter  $\beta$  and  $h'$  nor an unambiguous assignment. This ill-posed problem is also mentioned in Lyakhov et al. (2018), emphasizing that the results should be treated cautiously. However, we can draw from Figure 13 that  $\beta$  increases/decreases during the SSW (positive amplitude anomaly by  $\sim 5\text{--}6$  dB)/ES (negative amplitude anomaly by  $\sim 4\text{--}5$  dB) period, which supports the here presented theory. Due to the ambiguity, we cannot clearly assign the amplitude changes during SSW/ES to one effective reflection height  $h'$ . Nevertheless, it is possible to reproduce the amplitude changes during the SSW/ES event with modifications of  $\beta$  and  $h'$  described in the assumed mechanism (Figure 12). Figure 14 shows the reproduced temporal variation of the amplitude anomaly during the SSW/ES event in 2009 and the associated  $\beta$  and  $h'$  pairs taken from the parameter space for the amplitude anomaly (Figure 13).

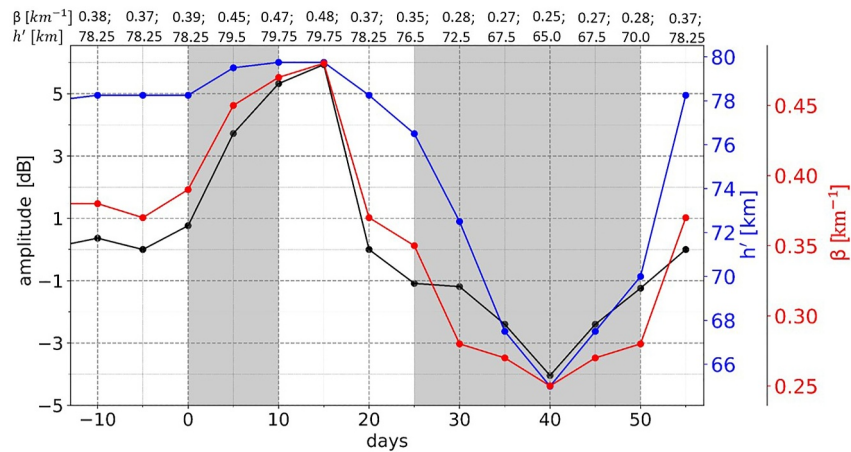


**Figure 14.** Temporal variation of the amplitude anomalies (in black) from the LWPC parameter space during a SSW/ES event. Amplitudes were determined by specific  $\beta$  (in red) and  $h'$  (in blue) pairs, in accordance with the proposed mechanism in Figure 12. The gray shaded areas mark the approximate SSW period (0–10 days) and the ES period (25–50 days).

Consistent with the assumed mechanism, the positive amplitude anomalies during the SSW period are related to increased  $\beta$  and  $h'$ , and the negative amplitude anomalies are linked to decreased  $\beta$  and  $h'$ . Be aware that ambiguity makes it possible to reproduce a similar amplitude anomaly variation with other  $\beta$  and  $h'$  pairs.

Pal et al. (2017) investigates the impact of the SSW event 2009 on the VLF signal. They analyzed the VLF signal amplitude of four different Tx-Rx combinations, from which the link from NRK to Kiel is the pathway that matches the most with the here-considered link from NRK-NYA. The comparison of the daytime amplitude variations shows an agreement in terms of an amplitude increase during the SSW. The ES period accompanying amplitude decrease is also notable in Pal et al. (2017) (their Figure 4, top panel), but it is not discussed in detail further. They concluded, that the stratospheric and mesospheric (with 2–3 days delay) temperature variation and the mesospheric pressure change are in good agreement with the daytime VLF signal. This roughly matches our observations, whereas differences may occur due to different data sources (they use SABER temperature measurements, we use MLS temperature) and different considered regions (they average over the north Atlantic sector, we along the pathway). With the help of LWPC test runs, they concluded that the electron density must be increased by up to 75% and the collision frequency must be slightly increased by 5% during the SSW period to obtain similar amplitude variations in the simulations as in the VLF measurements. Note, their result is contrary to ours as we stated that the amplitude increases during the SSW period due to a decrease in the electron density leading to a larger  $\beta$  and  $h'$ . We derived amplitude anomalies from the parameter space for the link NRK-NYA, while Pal et al. (2017) simulated the VLF amplitude for the for the Tx-Rx link from NRK-Kiel with different anomalies of the electron density profile and the collision frequency during the SSW in 2009. For the simulations, they used the electron-ion density from the International Reference Ionosphere (IRI-2012) model (Bilitza et al., 2011) along the propagation path and the collision frequency presented in Kelleys (2009), which has an indirect dependency on the temperature, for the LWPC simulations. Be aware that we used the collision frequency from Vuthaluru et al. (2002) with a direct dependency on the temperature. Different equations for the collision frequency can be one reason for the differences in the results. Furthermore, the contrasting results show how carefully the LWPC data should be evaluated due to their ambiguity. In addition to the ill-posed problem of the LWPC results, the electron density profile also plays a crucial role as an input parameter for the simulations. It can cause significant deviations from the measured VLF signal amplitude.

Thomson et al. (2022) fulfilled various LWPC simulations with the electron density profiles from IRI-2016 and FIRI-2018 (Faraday-International Reference Ionosphere) and compared them with VLF- and rocket measurements. They concluded that the D-region description in the FIRI-2018 model is a significant advance from the earlier IRI-2016 model. Nevertheless, they found that the calculated VLF amplitudes using FIRI-2018 electron density profiles are in low agreement with the measured VLF amplitudes for the high mid-latitude path from DHO (Rauderfehn, Germany) to ESK (Eskdalemuir, Finland). As a possible reason for the low agreement, they suspected the fact that the FIRI-2018 model does not fully recognize a greater number of electrons at lower altitudes



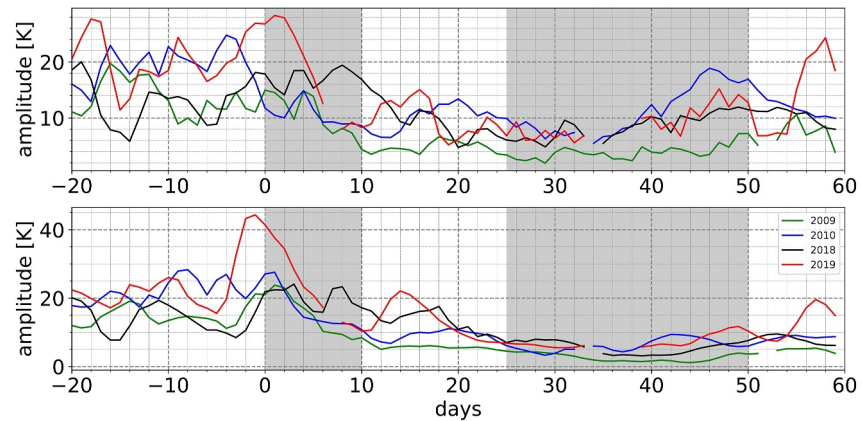


**Figure 15.** Stationary wave amplitude in the mesosphere (65–75 km, upper panel) and stratosphere (30–40 km, lower panel) computed for the latitude range 60–80°N. The gray shaded areas mark the approximate SSW period (0–10 days) and the ES period (25–50 days).

(<70 km) generated by galactic cosmic rays at these mid-high latitudes. For a path in lower latitudes (20°N), the LWPC simulation matches better with the VLF measurements; however, only during solar zenith angles (SZA) < 85°. The here-considered SSW/ES events usually occur in winter in high latitudes. LWPC simulations with FIRI-2018 electron density profiles are presumably unreliable due to too high SZA and the latitudinal limitation of FIRI-2018 (<60°). In addition, the winter shows a high degree of variability in temperature, wind, and chemistry due to increased wave activity, causing electron density modification, which is not considered in the FIRI-2018 model.

#### 4.2. Causes for the Different VLF Signal Amplitude Variation During the SSW/ES Event 2019

While the VLF signal variations during the three SSW/ES events in winter 2009, 2010, and 2018 are quite similar, the amplitude variation for the SSW/ES event in winter 2019 distinguished significantly (Figures 6 and 10a). The difference may be caused by the enhanced NO concentration, which occurs around 15 days before the MOD-SSW. In general, the NO concentration in the winter of 2019 is larger than the average. The NO increase presumably has a geomagnetic origin, as enhanced Kp, Ap, AE, and DST indices indicate (Figure 8). Clilverd et al. (2006) discussed the origin of wintertime NO around an SSW event in January 2004. Since, during that time, there wasn't an EPP event or elevated geomagnetic or solar activity, they excluded in situ NO production. They assumed that the NO was produced by low energy precipitation (LEPP) in auroral altitudes (~120 km) and descended in the presence of an enhanced polar vortex due to an associated downward transport. Similar to Clilverd et al. (2006), we cannot identify a clear origin for the enhanced NO concentration around 15 days before the MOD-SSW in 2019. One possible explanation could be that the increased geomagnetic indices approximately 50–45 days before MOD-SSW 2019 indicate a LEPP, which produced NO in auroral altitudes. As time progresses, the NO descends from auroral altitudes into the mesosphere, resulting in the observed NO enhancement 15 days before the MOD-SSW.

Similar to the ES effect (cf. Section 4.1), the observed NO infusion before the SSW event 2019 might increase the lower ionospheric electron density, resulting in a faded vertical density profile. Thus, the sharpness and the reflection height are reduced, which might prevent the increase of VLF signal amplitude as observed during the SSW period for the other three events in 2009, 2010, and 2018.

In addition, the temperature and zonal wind during the SSW/ES period in winter 2019 show a wave signature, particularly pronounced a few days after the MOD-SSW (Figure 7). Schmitter (2011) described how VLF/LF signal amplitude variations are modified by planetary wave-modulated collision frequency and electron density profiles. We used the stationary wave amplitude as a proxy for the wave activity. The stationary wave amplitude was deduced from a wave fit of the temperature retrieved from MLS measurements along the latitudinal circle, averaged between 60° and 80°N. Indeed, some unique features in the mesosphere during the SSW/ES event 2019 are notable in the stationary wave amplitude. It reaches with ~28 K around 20 days before and 2 days after the MOD-SSW the highest values in comparison with the other three events, as shown in the upper panel in Figure 15.

The stationary wave amplitude for all four SSW/ES events in the mesosphere from 20 days before until 10 days after the MOD-SSW is larger than during the ES period, whereas the high stationary wave amplitudes in 2019 stand out. We observe enhanced stationary wave amplitudes around the MOD-SSW in the stratosphere for all four events, with a maximum amplitude of  $\sim 42$  K during the MOD-SSW in 2019 (lower panel in Figure 15). Furthermore, the stationary wave amplitude for the event in 2019 is increased 10–20 days after the MOD-SSW in the stratosphere as well as in the mesosphere.

Stationary planetary waves contribute to the wave driving, which causes a meridional circulation in the stratosphere from the equator to the pole, the Brewer-Dobson circulation (BDC) (Cohen et al., 2014). The downwelling branch of the BDC in the polar regions causes a warming of the polar vortex. Additional warming is caused by the mixing of inside polar vortex air masses with air and chemical trace gases (e.g., ozone) from the outside by the BDC (Asikainen et al., 2020). Thus, increased stationary wave amplitudes lead to increased temperatures and trace gas concentrations within the polar vortex. The stationary wave amplitude during the winter of 2019 is larger than during the other considered years, presumably causing additional polar vortex disturbances, resulting in the differences in the temperature, zonal wind, and minor constituent variations during the winter of 2019 and of the average.

Note that the SSW event in 2019 starts at the end of December 2018 (MOD-SSW:  $-8$  DOY 2019, cf. Table 1), at least 4 weeks earlier than the other three investigated events here. Due to the early occurrence around the turn of 2018/2019, there may also be different prevailing conditions in terms of illumination of the Tx-Rx pathway, which might affect the VLF signal (Kozakova et al., 2023). Since there do not occur other SSW/ES events as early as in the winter 2019 during the data coverage of the VLF signal, we are not able to make comparisons and draw conclusions regarding the illumination influence on VLF signal variation during the SSW/ES event. This issue is worth further investigation.

We assume that the combination of the wave-driven atmospheric differences and the enhanced NO concentration with a presumably geomagnetic origin during winter 2019 likely modifies the collision frequency and electron density profiles, which is notable in the differences of the VLF signal amplitude during the 2019 SSW/ES event between the average of the other three SSW/ES events shown in Figure 10a.

## 5. Summary and Conclusion

Here, we study the daytime VLF signal amplitude variation from the high latitude link NRK-NYA belonging to the AARDDVARK network during four SSW/ES events under low to moderate solar conditions. The SSW/ES event occurrence time varies between the four events. For better comparability, we centered the time series of the VLF signal amplitudes and the primary atmospheric drivers (temperature, zonal wind, ozone, water vapor, and nitric oxide) on the mesospheric onset day (MOD-SSW) of each event, representing the day when the SSW event starts in the mesosphere.

Since the VLF signal is reflected within mesospheric ranges, it was essential to center the time series of the VLF signal amplitudes and the driving parameters on the MOD-SSW. Until now, there has been no definition of the start and length of an SSW or ES event in the mesosphere. Previous studies use the definition by the temperature and zonal wind at 10 hPa ( $\sim 30$  km) (Baldwin et al., 2021) or also polar vortex conditions (split, displaced or undisturbed) in 10 hPa (Charlton & Polvani, 2007). The difficulty of capturing SSW caused perturbations in higher altitudes was already mentioned in Greer et al. (2013). Thus, the MOD-SSW and MOD-ES defined here could also be valuable for other studies focusing on the MLT region.

With the help of the centered temporal variations of the VLF signal amplitude and the atmospheric drivers during the SSW/ES period, simulations of the electron density profile by the Sodankylä Ion and Neutral Chemistry Model, and amplitude simulations by LWPC, we could derive the following main findings:

1. *Average VLF signal amplitude signature:* Three of the four investigated events show a very similar VLF amplitude signature during the SSW/ES events, manifested by an amplitude increase during the SSW period and decreased amplitudes during the ES period.
2. *Possible mechanism:* During the SSW period, the recombination rate is increased due to the lower mesospheric temperatures and the increased water vapor, which probably increases the sharpness  $\beta$  of the vertical electron density profile. Moreover, the decreased mesospheric temperatures lead to a decrease in the collision frequency, causing a reduced absorption of the VLF signal. The increase in the vertical electron density profile

gradient and the reduction in the collision frequency lead to an increase in the VLF signal amplitude during the SSW period. Contrary processes work during the ES period. Reduced recombination due to increased temperatures and a decrease in water vapor, combined with an increased collision frequency due to the higher mesospheric temperatures, results in a lower gradient of the vertical electron density profile and increased absorption of the VLF signal. In addition, the significant increase in NO density caused by the downwelling associated with the ES period leads to an increase in electron density at lower altitudes, further attenuating the vertical electron density profile and likely reducing the effective reflection height  $h'$ . Thus, the decrease in the gradient of the vertical electron profile, the effective reflection height, and the collision frequency increase cause a decrease in the VLF signal amplitude during the ES period. The scheme of the assumed mechanism is shown in Figure 12. Note that we confirmed our results with LWPC. However, our results are ambiguous as solving the  $\beta$  and  $h'$  is an ill-posed problem.

3. *Reason for difference:* The VLF amplitude variation during the SSW/ES event in winter 2019 does not match the signature of the other three events. There is neither a significant amplitude increase during the SSW period, only a weaker amplitude increase, which occurs almost 14 days later than the average, nor are there decreased amplitudes during the ES period. In addition to the general characteristics of an SSW/ES event, there was a significant increase in the NO concentration before the SSW in 2019, likely related to a weak geomagnetic storm. Furthermore, the SSW/ES 2019 event shows a larger stationary wave amplitude than during the other three SSW/ES events. From this, we conclude that the average signature during an SSW/ES event can be disturbed or superimposed by effects caused by solar and geomagnetic events (e.g., solar flares, geomagnetic storms) as well as atmospheric waves, which may modify temperature, dynamic and chemistry and so the D-region ionization.

### Data Availability Statement

All data used in this study are freely available. VLF signal amplitude data from the AARDDVARK Network (2009) were downloaded from <https://psddb.nerc-bas.ac.uk>. The link leads to a landing page with a search mask in the upper right corner. The receiver station must be entered into the search mask to access the data. Here, choosing the year and the data class ULTRA leads to an information page from where you can access data to all transmitter variations to the chosen receiver for the determined year under the term View this Data. Aura MLS temperature L2 data sets are available from Schwartz et al. (2020b), geopotential height data sets are available from Schwartz et al. (2020a) and water vapor data sets are available from Lambert et al. (2020). The SD-WACCM-X data sets are available from Gasperini (2020). The level 2 ODIN-SMR data are publicly accessible at <http://odin.rss.chalmers.se/level2> (OdinSMR, 2021). NASA/GSFC's OMNI data sets were downloaded from <https://omniweb.gsfc.nasa.gov/form/dx1.html> (OMNIWeb, 2024).

### Acknowledgments

We thank all AARDDVARK members of the Konsortia for maintaining the VLF receiver and the provision of data. We also thank the MLS team for providing the data sets used in this study and the Jet Propulsion Laboratory/NASA for providing access to the Aura/MLS level 2 retrieval products. Furthermore, we would like to thank UCAR/NCAR—Climate and Global Dynamics Laboratory for providing the SD-WACCM-X data sets used in this study. The work of P. T. Verronen has been supported by the Research Council of Finland (Grant 354331, GERACLIS). Open Access funding enabled and organized by Projekt DEAL.

### References

- AARDDVARK Network. (2009). VLF radio waves observations in Arctic and Antarctic region [Dataset]. Retrieved from <https://psddb.nerc-bas.ac.uk>
- Andrews, D. G., Taylor, F. W., & McIntyre, M. E. (1987). The influence of atmospheric waves on the general circulation of the middle atmosphere [and discussion]. *Philosophical Transactions of the Royal Society of London - Series A: Mathematical and Physical Sciences*, 323(1575), 693–705. Retrieved from <http://www.jstor.org/stable/38143>
- Asikainen, T., Salminen, A., Maliniemi, V., & Mursula, K. (2020). Influence of enhanced planetary wave activity on the polar vortex enhancement related to energetic electron precipitation. *Journal of Geophysical Research: Atmospheres*, 125(9), e2019JD032137. <https://doi.org/10.1029/2019JD032137>
- Bajčetić, J., Nina, A., Čadež, V. M., & Todorović, B. M. (2017). Ionospheric D-region temperature relaxation and its influences on radio signal propagation after solar x-flares occurrence. *Thermal Science*, 19, 299–303. Retrieved from <https://api.semanticscholar.org/CorpusID:54606727>
- Baldwin, M. P., Ayzargüena, B., Birner, T., Butchart, N., Butler, A. H., Charlton-Perez, A. J., et al. (2021). Sudden stratospheric warmings. *Reviews of Geophysics*, 59(1), e2020RG000708. <https://doi.org/10.1029/2020RG000708>
- Barr, R., Jones, D., & Rodger, C. (2000). ELF and VLF radio waves. *Journal of Atmospheric and Solar-Terrestrial Physics*, 62(17), 1689–1718. [https://doi.org/10.1016/S1364-6826\(00\)00121-8](https://doi.org/10.1016/S1364-6826(00)00121-8)
- Belrose, J. S. (1967). The “Berlin” warming. *Nature*, 214(5089), 660–664. <https://doi.org/10.1038/214660a0>
- Bilitza, D., McKinnell, L.-A., Reinisch, B., & Fuller-Rowell, T. (2011). The international reference ionosphere today and in the future. *Journal of Geodesy*, 85(12), 909–920. <https://doi.org/10.1007/s00190-010-0427-x>
- Brakebusch, M., Randall, C. E., Kinnison, D. E., Tilmes, S., Santee, M. L., & Manney, G. L. (2013). Evaluation of whole atmosphere community climate model simulations of ozone during arctic winter 2004–2005. *Journal of Geophysical Research: Atmospheres*, 118(6), 2673–2688. <https://doi.org/10.1002/jgrd.50226>
- Chandran, A., Collins, R., & Harvey, V. (2014). Stratosphere-mesosphere coupling during stratospheric sudden warming events. *Advances in Space Research*, 53(9), 1265–1289. <https://doi.org/10.1016/j.asr.2014.02.005>



- Chandran, A., Collins, R. L., Garcia, R. R., & Marsh, D. R. (2011). A case study of an elevated stratopause generated in the whole atmosphere community climate model. *Geophysical Research Letters*, *38*(8). <https://doi.org/10.1029/2010GL046566>
- Chandran, A., Collins, R. L., Garcia, R. R., Marsh, D. R., Harvey, V. L., Yue, J., & dela Torre, L. (2013). A climatology of elevated stratopause events in the whole atmosphere community climate model. *Journal of Geophysical Research: Atmospheres*, *118*(3), 1234–1246. <https://doi.org/10.1002/jgrd.50123>
- Chandran, A., Garcia, R. R., Collins, R. L., & Chang, L. C. (2013). Secondary planetary waves in the middle and upper atmosphere following the stratospheric sudden warming event of January 2012. *Geophysical Research Letters*, *40*(9), 1861–1867. <https://doi.org/10.1002/grl.50373>
- Charlton, A. J., & Polvani, L. M. (2007). A new look at stratospheric sudden warmings. Part I: Climatology and modeling benchmarks. *Journal of Climate*, *20*(3), 449–469. <https://doi.org/10.1175/JCLI3996.1>
- Charney, J. G., & Drazin, P. G. (1961). Propagation of planetary-scale disturbances from the lower into the upper atmosphere. *Journal of Geophysical Research*, *66*(1), 1896–1977. <https://doi.org/10.1029/JZ066i001p00083>
- Clilverd, M. A., Rodger, C. J., Thomson, N. R., Brundell, J. B., Ulich, T., Lichtenberger, J., et al. (2009). Remote sensing space weather events: Antarctic-Arctic Radiation-belt (dynamic) Deposition-VLF Atmospheric Research consortium network. *Space Weather-The International Journal of Research and Applications*, *7*(S04001). <https://doi.org/10.1029/2008SW000412>
- Clilverd, M. A., Seppälä, A., Rodger, C. J., Thomson, N. R., Lichtenberger, J., & Steinbach, P. (2007a). Temporal variability of the descent of high-altitude NO<sub>x</sub> inferred from ionospheric data. *Journal of Geophysical Research*, *112*(A9). <https://doi.org/10.1029/2006JA012085>
- Clilverd, M. A., Seppälä, A., Rodger, C. J., Thomson, N. R., Lichtenberger, J., & Steinbach, P. (2007b). Temporal variability of the descent of high-altitude NO<sub>x</sub> inferred from ionospheric data. *Journal of Geophysical Research*, *112*(A9). <https://doi.org/10.1029/2006JA012085>
- Clilverd, M. A., Seppälä, A., Rodger, C. J., Verronen, P. T., & Thomson, N. R. (2006). Ionospheric evidence of thermosphere-to-stratosphere descent of polar NO<sub>x</sub>. *Geophysical Research Letters*, *33*(L19811). <https://doi.org/10.1029/2006GL026727>
- Cohen, N. Y., Gerber, E. P., & Bühler, O. (2014). What drives the Brewer–Dobson circulation? *Journal of the Atmospheric Sciences*, *71*(10), 3837–3855. <https://doi.org/10.1175/JAS-D-14-0021.1>
- Danilov, A. (1981). Physics of the D region and forecasting the propagation of radio waves (review). *Radiophys Quantum Electron*, *24*(10), 793–813. <https://doi.org/10.1007/BF01034181>
- Ferguson, J. A. (1998). Computer programs for assessment of long-wavelength radio communications, version 2.0: User's guide and source files Technical Document. Retrieved from <https://api.semanticscholar.org/CorpusID:53741397>
- Fritts, D. C., & Alexander, M. J. (2003). Gravity wave dynamics and effects in the middle atmosphere. *Reviews of Geophysics*, *41*(1). <https://doi.org/10.1029/2001RG000106>
- Gasperini, F. (2020). Cesm run sd-waccm-xv2.1 and sdwaccmx12.04.2020v5 [Dataset]. *NCAR Climate Data Gateway*. Retrieved from [https://www.earthsystemgrid.org/dataset/ucar.cgd.cesm4.SD-WACCM-X\\_v2.1.html](https://www.earthsystemgrid.org/dataset/ucar.cgd.cesm4.SD-WACCM-X_v2.1.html)
- Greer, K., Thayer, J. P., & Harvey, V. L. (2013). A climatology of polar winter stratopause warmings and associated planetary wave breaking. *Journal of Geophysical Research: Atmospheres*, *118*(10), 4168–4180. <https://doi.org/10.1002/jgrd.50289>
- Gruber, D. P., Šulić, D. M., & Žigman, V. (2008). Classification of x-ray solar flares regarding their effects on the lower ionosphere electron density profile. *Annales Geophysicae*, *26*(7), 1731–1740. <https://doi.org/10.5194/angeo-26-1731-2008>
- Gulyaeva, T. (2017). Ranking ICME'S efficiency for geomagnetic and ionospheric storms and risk of false alarms. *Journal of Atmospheric and Solar-Terrestrial Physics*, *164*, 39–47. <https://doi.org/10.1016/j.jastp.2017.07.021>
- Hunsucker, R. D., & Hargreaves, J. K. (2002). *The high-latitude ionosphere and its effects on radio propagation*. Cambridge University Press.
- Jia, J., Murberg, L. E., Løvset, T., Orsolini, Y. J., Espy, P. J., Zeller, L. C. G., et al. (2024). Energetic particle precipitation influences global secondary ozone distribution. *Communications Earth & Environment*, *5*(1), 270. <https://doi.org/10.1038/s43247-024-01419-2>
- Karami, K., Borchert, S., Eichinger, R., Jacobi, C., Kuchar, A., Mehrdad, S., et al. (2023). The climatology of elevated stratopause events in the UA-ICON model and the contribution of gravity waves. *Journal of Geophysical Research: Atmospheres*, *128*(7), e2022JD037907. <https://doi.org/10.1029/2022JD037907>
- Kelleys, M. C. (2009). The Earth's ionosphere. *Elsevier*, *96*(2).
- Kozakova, E. N., Ryakhovskiy, I. A., Poklad, Y. V., Gavrilov, B. G., Ermak, V. M., & Achkasov, N. S. (2023). Influence of path illumination on the amplitude characteristics of VLF signals. *Annales Geophysicae*, *63*(2), 127–135. <https://doi.org/10.1134/S0016793222600850>
- Lambert, A., Read, W., & Livesey, N. (2020). MLS/Aura Level 2 Water Vapor (H<sub>2</sub>O) Mixing Ratio V005 [Dataset]. *Greenbelt, MD, USA, Goddard Earth Sciences Data and Information Services Center (GES DISC)*. <https://doi.org/10.5067/Aura/MLS/DATA2508>
- Larsen, T. (1971). Short path VLF phase and amplitude measurements during a stratospheric warming in February 1969. *Journal of Atmospheric and Terrestrial Physics*, *33*(8), 1251–1256. [https://doi.org/10.1016/0021-9169\(71\)90111-5](https://doi.org/10.1016/0021-9169(71)90111-5)
- Limpasuvan, V., Orsolini, Y. J., Chandran, A., Garcia, R. R., & Smith, A. K. (2016). On the composite response of the MLT to major sudden stratospheric warming events with elevated stratopause. *Journal of Geophysical Research: Atmospheres*, *121*(9), 4518–4537. <https://doi.org/10.1002/2015JD024401>
- Limpasuvan, V., Richter, J. H., Orsolini, Y. J., Stordal, F., & Kvissel, O.-K. (2012). The roles of planetary and gravity waves during a major stratospheric sudden warming as characterized in waccm. *Journal of Atmospheric and Solar-Terrestrial Physics*, *78*–79, 84–98. <https://doi.org/10.1016/j.jastp.2011.03.004>
- Liu, H.-L. (2025). Transport of nitric oxide in the winter mesosphere and lower thermosphere. *Geophysical Research Letters*, *52*(3), e2024GL113027. <https://doi.org/10.1029/2024GL113027>
- Liu, H.-L., Bardeen, C. G., Foster, B. T., Lauritzen, P., Liu, J., Lu, G., et al. (2018). Development and validation of the whole atmosphere community climate model with thermosphere and ionosphere extension (WACCM-X 2.0). *Journal of Advances in Modeling Earth Systems*, *10*(2), 381–402. <https://doi.org/10.1002/2017MS001232>
- Livesey, N. J., Santee, M. L., & Manney, G. L. (2015). A match-based approach to the estimation of polar stratospheric ozone loss using aurora microwave limb sounder observations. *Atmospheric Chemistry and Physics*, *15*(17), 9945–9963. <https://doi.org/10.5194/acp-15-9945-2015>
- Loewe, C. A., & Prölss, G. W. (1997). Classification and mean behavior of magnetic storms. *Journal of Geophysical Research*, *102*(A7), 14209–14213. <https://doi.org/10.1029/96JA04020>
- Luo, J., Ying, K., & Bai, J. (2005). Savitzky–Golay smoothing and differentiation filter for even number data. *Signal Processing*, *85*(7), 1429–1434. <https://doi.org/10.1016/j.sigpro.2005.02.002>
- Lyakhov, A. N., Korsunskaya, J. A., Gavrilov, B. G., Ryakhovskiy, I. A., Bisyarin, M. A., Kirillov, V. V., et al. (2018). Verification of the empirical lower ionosphere models on VLF observations at midlatitude mikhnevo geophysical observatory. In *Atmospheric and ocean optics*. Retrieved from <https://api.semanticscholar.org/CorpusID:134966814>
- Macotela, E. L., Clilverd, M., Renkwitz, T., Chau, J., Manninen, J., & Banyas, D. (2021). Spring-fall asymmetry in VLF amplitudes recorded in the north atlantic region: The fall-effect. *Geophysical Research Letters*, *48*(16). <https://doi.org/10.1029/2021GL094581>

- Manney, G. L., Krüger, K., Sabutis, J. L., Sena, S. A., & Pawson, S. (2005). The remarkable 2003–2004 winter and other recent warm winters in the arctic stratosphere since the late 1990s. *Journal of Geophysical Research*, *110*(D4). <https://doi.org/10.1029/2004JD005367>
- Manney, G. L., Schwartz, M. J., Krüger, K., Santee, M. L., Pawson, S., Lee, J. N., et al. (2009). Aura microwave limb sounder observations of dynamics and transport during the record-breaking 2009 Arctic stratospheric major warming. *Geophysical Research Letters*, *36*(12). <https://doi.org/10.1029/2009GL038586>
- Marsh, D. R., Mills, M. J., Kinnison, D. E., Lamarque, J.-F., Calvo, N., & Polvani, L. M. (2013). Climate change from 1850 to 2005 simulated in cesm1(WACCM). *Journal of Climate*, *26*(19), 7372–7391. <https://doi.org/10.1175/JCLI-D-12-00558.1>
- Matsuno, T. (1971). A dynamical model of the stratospheric sudden warming. *Journal of the Atmospheric Sciences*, *28*(8), 1479–1494. [https://doi.org/10.1175/1520-0469\(1971\)028<1479:ADMOTS>2.0.CO;2](https://doi.org/10.1175/1520-0469(1971)028<1479:ADMOTS>2.0.CO;2)
- McCormick, J. C., & Cohen, M. B. (2021). A new four-parameter D-region ionospheric model: Inferences from lightning-emitted VLF signals. *Journal of Geophysical Research: Space Physics*, *126*(12). <https://doi.org/10.1029/2021JA029849>
- Mitra, A. (1978). The D-region of the ionosphere. *Endeavour*, *2*(1), 12–21. [https://doi.org/10.1016/0160-9327\(78\)90028-5](https://doi.org/10.1016/0160-9327(78)90028-5)
- Mondal, S. K., Chakrabarti, S. K., & Sasmal, S. (2012). Detection of ionospheric perturbation due to a soft gamma ray repeater sgr j1550-5418 by very low frequency radio waves. *Astrophysics and Space Science*, *341*(2), 259–264. <https://doi.org/10.1007/s10509-012-1131-5>
- Mondal, S. K., Pal, S., Sen, A., Rahaman, M., & Midya, S. K. (2021). Long-lasting disturbances in the mid-latitude sub-ionospheric VLF radio signals due to the super geomagnetic storm of 17 March 2015. *Advances in Space Research*, *68*(6), 2295–2308. <https://doi.org/10.1016/j.asr.2021.04.044>
- Nwankwo, V. U. J., Denig, W., Chakrabarti, S. K., Ogunmodimu, O., Ajakaiye, M. P., Fatokun, J. O., et al. (2022). Diagnostic study of geomagnetic storm-induced ionospheric changes over very low-frequency signal propagation paths in the mid-latitude D region. *Annales Geophysicae*, *40*(4), 433–461. <https://doi.org/10.5194/angeo-40-433-2022>
- OdinSMR. (2021). Level2 data dashboard [Dataset]. Retrieved from <http://odin.rss.chalmers.se/level2>
- Okui, H., Sato, K., Koshin, D., & Watanabe, S. (2021). Formation of a mesospheric inversion layer and the subsequent elevated stratopause associated with the major stratospheric sudden warming in 2018/19. *Journal of Geophysical Research: Atmospheres*, *126*(18), e2021JD034681. <https://doi.org/10.1029/2021JD034681>
- OMNIWeb. (2024). Data dashboard [Dataset]. Retrieved from <https://omniweb.gsfc.nasa.gov/form/dx1.html>
- Pal, S., Hobara, Y., Chakrabarti, S. K., & Schnoor, P. W. (2017). Effects of the major sudden stratospheric warming event of 2009 on the subionospheric very low frequency/low frequency radio signals. *Journal of Geophysical Research: Space Physics*, *122*(7), 7555–7566. <https://doi.org/10.1002/2016JA023813>
- Pérot, K., & Orsolini, Y. J. (2021). Impact of the major ssws of February 2018 and January 2019 on the middle atmospheric nitric oxide abundance. *Journal of Atmospheric and Solar-Terrestrial Physics*, *218*, 105586. <https://doi.org/10.1016/j.jastp.2021.105586>
- Randall, C. E., Harvey, V. L., Siskind, D. E., France, J., Bernath, P. F., Boone, C. D., & Walker, K. A. (2009). NO<sub>x</sub> descent in the arctic middle atmosphere in early 2009. *Geophysical Research Letters*, *36*(18). <https://doi.org/10.1029/2009GL039706>
- Richmond, A. D., Ridley, E. C., & Roble, R. G. (1992). A thermosphere/ionosphere general circulation model with coupled electrodynamics. *Geophysical Research Letters*, *19*(6), 601–604. <https://doi.org/10.1029/92GL00401>
- Rienecker, M. M., Suarez, M. J., Gelaro, R., Todling, R., Bacmeister, J., Liu, E., et al. (2011). MERRA: NASA'S modern-era retrospective analysis for research and applications. *Journal of Climate*, *24*(14), 3624–3648. <https://doi.org/10.1175/JCLI-D-11-00015.1>
- Rozanov, E., Calisto, M., Egorova, T., Peter, T., & Schmutz, W. (2012). Influence of the precipitating energetic particles on atmospheric chemistry and climate. *Surveys in Geophysics*, *33*(3), 483–501. <https://doi.org/10.1007/s10712-012-9192-0>
- Rüfenacht, R., Baumgarten, G., Hildebrand, J., Schranz, F., Matthias, V., Stober, G., et al. (2018). Intercomparison of middle-atmospheric wind in observations and models. *Atmospheric Measurement Techniques*, *11*(4), 1971–1987. <https://doi.org/10.5194/amt-11-1971-2018>
- Sassi, F., Liu, H.-L., Ma, J., & Garcia, R. R. (2013). The lower thermosphere during the northern hemisphere winter of 2009: A modeling study using high-altitude data assimilation products in WACCM-X. *Journal of Geophysical Research: Atmospheres*, *118*(16), 8954–8968. <https://doi.org/10.1002/jgrd.50632>
- Scheffler, J., Ayarzagüena, B., Orsolini, Y. J., & Langematz, U. (2022). Elevated stratopause events in the current and a future climate: A chemistry-climate model study. *Journal of Atmospheric and Solar-Terrestrial Physics*, *227*, 105804. <https://doi.org/10.1016/j.jastp.2021.105804>
- Schmitter, E. D. (2011). Remote sensing planetary waves in the midlatitude mesosphere using low frequency transmitter signals. *Annales Geophysicae*, *29*(7), 1287–1293. <https://doi.org/10.5194/angeo-29-1287-2011>
- Schneider, H., Wendt, V., Banys, D., Clilverd, M., & Raita, T. (2024). Processing of VLF amplitude measurements: Deduction of a quiet time seasonal variation. *Radio Science*, *59*(2), e2023RS007834. <https://doi.org/10.1029/2023RS007834>
- Schwartz, M., Livesey, N., & Read, W. (2020a). MLS/Aura Level 2 GPH V005 [Dataset]. *Greenbelt, MD, USA, Goddard Earth Sciences Data and Information Services Center (GES DISC)*. <https://doi.org/10.5067/Aura/MLS/DATA2507>
- Schwartz, M., Livesey, N., & Read, W. (2020b). MLS/Aura Level 2 Temperature V005 [Dataset]. *Greenbelt, MD, USA, Goddard Earth Sciences Data and Information Services Center (GES DISC)*. <https://doi.org/10.5067/Aura/MLS/DATA2520>
- Sen, A., Pal, S., & Mondal, S. K. (2024). Mid-latitude ionospheric disturbances during the major sudden stratospheric warming event of 2018 observed by sub-ionospheric VLF/LF signals. *Advances in Space Research*, *73*(1), 767–779. <https://doi.org/10.1016/j.asr.2023.10.025>
- Sinnhuber, M., Arras, C., Bender, S., Funke, B., Liu, H., Marsh, D. R., et al. (2024). Thermospheric nitric oxide no during solar minimum modulated by O/O<sub>2</sub> ratio and thermospheric transport and mixing. *EGU sphere*, *2024*, 1–29.
- Sinnhuber, M., Nieder, H., & Wieters, N. (2012). Energetic particle precipitation and the chemistry of the mesosphere/lower thermosphere. *Surveys in Geophysics*, *33*(6), 1281–1334. <https://doi.org/10.1007/s10712-012-9201-3>
- Siskind, D. E., Zawdie, K. A., Sassi, F., Drob, D. P., & Friedrich, M. (2018). An intercomparison of VLF and sounding rocket techniques for measuring the daytime D region ionosphere: Theoretical implications. *Journal of Geophysical Research: Space Physics*, *123*(10), 8688–8697. <https://doi.org/10.1029/2018JA025807>
- Smith-Johnsen, C., Marsh, D. R., Smith, A. K., Tyssøy, H. N., & Maliniemi, V. (2022). Mesospheric nitric oxide transport in WACCM. *Journal of Geophysical Research: Space Physics*, *127*(3), e2021JA029998. <https://doi.org/10.1029/2021JA029998>
- Solomon, S., Crutzen, P. J., & Roble, R. G. (1982). Photochemical coupling between the thermosphere and the lower atmosphere: 1. Odd nitrogen from 50 to 120 km. *Journal of Geophysical Research*, *87*(C9), 7206–7220. <https://doi.org/10.1029/JC087iC09p07206>
- Solovieva, M. S., & Shalimov, S. L. (2022). Disturbances in the lower ionosphere after the eruption of the Hunga-Tonga-Hunga-Ha'apai volcano on January 15, 2022, recorded by the subionospheric VLF radio signals. *Doklady Earth Sciences*, *507*(2), 1080–1084. <https://doi.org/10.1134/S1028334X22600840>
- Thomson, N. R., Clilverd, M., Brundell, J. B., & Rodger, C. (2021). Quiet night arctic ionospheric D region characteristics. *Journal of Geophysical Research: Space Physics*, *126*(4). <https://doi.org/10.1029/2020JA029043>

- Thomson, N. R., Clilverd, M. A., & Rodger, C. J. (2022). Ionospheric D region: VLF-measured electron densities compared with rocket-based FIRI-2018 model. *Journal of Geophysical Research: Space Physics*, *127*(11). <https://doi.org/10.1029/2022JA030977>
- Thrane, E., & Piggott, W. (1966). The collision frequency in the E- and D-regions of the ionosphere. *Journal of Atmospheric and Terrestrial Physics*, *28*(8), 721–737. [https://doi.org/10.1016/0021-9169\(66\)90021-3](https://doi.org/10.1016/0021-9169(66)90021-3)
- Turunen, E., Matveinen, H., Tolvanen, J., & Ranta, H. (1996). *Step handbook of ionospheric models* (Vol. 1). SCOSTEP Secretariat.
- Verronen, P. T., Seppälä, A., Clilverd, M. A., Rodger, C. J., Kyrölä, E., Enell, C.-F., et al. (2005). Diurnal variation of ozone depletion during the October–November 2003 solar proton events. *Journal of Geophysical Research*, *110*(A9), 0148–0227. <https://doi.org/10.1029/2004JA010932>
- Vuthaluru, R., Vincent, R., Holdsworth, D., & Reid, I. (2002). Collision frequencies in the D-region. *Journal of Atmospheric and Solar-Terrestrial Physics*, *64*(18), 2043–2054. [https://doi.org/10.1016/S1364-6826\(02\)00220-1](https://doi.org/10.1016/S1364-6826(02)00220-1)
- Wait, J. R. (1957). The mode theory of VLF ionospheric propagation for finite ground conductivity. *Proceedings of the IRE*, *45*(6), 760–767. <https://doi.org/10.1109/JRPROC.1957.278469>
- Wait, J. R., & Spies, K. P. (1964). *Characteristics of the earth-ionosphere waveguide for VLF radio waves*. National Bureau of Standards.
- Waters, J., Froidevaux, L., Harwood, R., Jarnot, R., Pickett, H., Read, W., et al. (2006). The Earth observing system microwave limb sounder (EOS MLS) on the aura satellite. *IEEE Transactions on Geoscience and Remote Sensing*, *44*(5), 1075–1092. <https://doi.org/10.1109/TGRS.2006.873771>
- Wenzel, D., Jakowski, N., Berdermann, J., Mayer, C., Valladares, C., & Heber, B. (2016). Global ionospheric flare detection system (GIFDS). *Journal of Atmospheric and Solar-Terrestrial Physics*, *138–139*, 233–242. <https://doi.org/10.1016/j.jastp.2015.12.011>
- Xu, W., Feng, J., Gu, X., Ni, B., Wang, S., Cheng, W., et al. (2024). Periodic oscillation of VLF transmitter signals measured in low and middle latitude regions. *Journal of Geophysical Research: Atmospheres*, *129*(10), e2023JD040225. <https://doi.org/10.1029/2023JD040225>
- Yamashita, C., England, S. L., Immel, T. J., & Chang, L. C. (2013). Gravity wave variations during elevated stratopause events using saber observations. *Journal of Geophysical Research: Atmospheres*, *118*(11), 5287–5303. <https://doi.org/10.1002/jgrd.50474>